Plasma Chemistry and Plasma Processing (2025) 45:843–871
https://doi.org/10.1007/s11090-025-10548-1

ORIGINAL PAPER

Plasma-Assisted Non-Oxidative Coupling of Methane: Effects of Bead Size Distribution and Operating Pressure in a Co-axial DBD

T. S. Larsen[1] · **J. A. Andersen**[1] · **J. M. Christensen**[1] · **A. Fateev**[1] · **M. Østberg**[2] · **E. Morais**[3] · **A. Bogaerts**[3] · **A. D. Jensen**[1]

Received: 26 July 2024 / Accepted: 27 January 2025 / Published online: 23 February 2025

Abstract
A co-axial packed-bed DBD reactor was used to conduct plasma-assisted non-oxidative coupling of methane (NOCM) utilizing glass beads as packing material at a fixed plasma power of 30 W. The influence on NOCM of five different bead size distributions (2000–5000 µm, 900–1100 µm, 425–600 µm, 212–300 µm, 150–212 µm) and operating pressure (1.2 bar, 1.7 bar) was investigated. The observed products consist of a mixture of saturated and unsaturated C_2–C_5 hydrocarbons. The conversion of methane decreased from 8.5 to 3.7% with decreasing bead size, while the selectivity towards unsaturated C_2 compounds increased from 16 to 50% with decreasing bead size. These reactor performance variations are associated with the transitional plasma dynamics and degree of partial discharging, as determined by characterization of non-ideal charge–voltage plots for the five tested glass bead sizes.

Keywords Non-oxidative coupling of CH_4 · Packed bed DBD reactor · Non-thermal plasma · Partial discharging · Plasma–packing interactions

Introduction

The detrimental consequences of the anthropogenic emissions of greenhouse gasses into the atmosphere have forced the global society to focus more on developing and implementing sustainable and green energy solutions. However, the intermittent character and fluctuating production capacity of such technologies impose a substantial need for efficient energy storage. This, as of now, remains unresolved due to several factors, including the inadequate matureness of existing storage technologies, coupled with the compelling need

---

✉ A. D. Jensen
aj@kt.dtu.dk

[1] Department of Chemical and Biochemical Engineering, Technical University of Denmark, Kgs. Lyngby, Denmark

[2] Topsoe A/S, Kgs. Lyngby, Denmark

[3] PLASMANT, Department of Chemistry, University of Antwerp, Wilrijk, Belgium

for a comprehensive advancement of the electrical grid stability and resilience [1, 2]. One possible solution, which is frequently highlighted as an efficient energy storage technology and an essential contributor to the energy storage challenge of renewables, is power-to-X (PtX). Converting renewably produced electricity into chemical energy carriers (hydrogen, ammonia, methanol, synthesis gas, hydrocarbons) is expected to increase significantly in the coming decades, and it advantageously equalizes the imbalance between energy supply and demand [3, 4]. One branch of reaction routes that has attracted considerable attention regarding conventional applications, as well as PtX, is the direct conversion of methane to value-added chemicals, such as synthesis gas, olefins, and aromatics, due to the abundant availability and economic upgrading potentials of methane [5–7]. Currently, the chemical industry's most widely used methane conversion technology is the indirect route, producing synthesis gas that requires very energy-intensive process steps (steam reforming or partial oxidation), followed by coupling reactions to long-chain hydrocarbons or to methanol. Therefore, significant research has been devoted to exploring catalysts and process conditions that effectively can activate the C–H bonds of methane and keep a high selectivity towards targeted C–C coupling reactions, to improve the direct conversion of methane for more efficient utilization. However, the direct non-oxidative coupling of methane (NOCM) has proven challenging, due to the inertness of the strong C–H bonds, where high-temperature conditions are required for activation, causing severe catalyst deactivation [8]. In contrast to conventional approaches, a promising technology that has proven to overcome the thermodynamic and kinetic barriers of NOCM is plasma technology [7, 9–11]. In non-thermal plasmas (NTP), the energy input is based on the acceleration and collisions of charge carriers due to the strong externally applied electric field, creating a very reactive environment consisting of free electrons, ions, radicals, excited species, besides ground-state molecules, under mild (low temperature) reaction conditions [12–14]. Moreover, the only energy input is electricity, which, when produced renewably, designates NTP as a promising alternative PtX technology for NOCM, accommodating the substantial need for efficient energy storage of renewables.

During the last century, NTP technologies were developed and already applied for industrial applications as the first ozone generation process. The most widely used NTP technology is the dielectric barrier discharge (DBD) reactor, often operated as a packed-bed reactor (PBR) [15]. In the recent decade, the application of packed-bed DBD plasma reactors loaded with catalysts (plasma catalysis) has been subjected to extensive research as a promising gas conversion technology, potentially combining the advantages of both catalysis and plasma technologies. The hybridization of combining plasma and catalysis has been proven in the existing literature to result in enhanced process outcomes that cannot be achieved by plasma or catalysis separately [16, 17]. These surplus effects are often referred to as synergistic effects, originating from the complex interplay between the plasma and the catalyst [18]. However, the abundant studies addressing the utilization possibilities and mechanisms of plasma catalysis as a promising new technology largely report inconsistent observations [19–24], showing this technology involves underlying complexities, particularly regarding the synergistic effects, which need clarification to achieve further advances. Irrespective of the unresolved difficulties, previous research agrees on and distinctly assigns some properties, like dielectric constant or roughness, of the packing material to have a prominent influence on the plasma dynamics in the bed zone [25, 26]. Several investigations have been aimed at assessing the effects of not only the dielectric constant, but also surface area, porosity, geometry, and packing efficiency, on the co-dependent mechanisms of plasma and packing material [21, 26–32]. Changes in these material properties, primarily in the dielectric constant, can significantly modify the plasma's electrical properties, enhancing the electric field in local contact points in the proximity of the packing material, attributed to polarization effects [32]. This, in turn, affects the streamer formation and propagation, and hence the chemical reactivity, dissociation, excitation, and ionization rates taking place in the plasma zone.

Previous work conducted prior to this study has investigated streamer dynamics in packed-bed DBD plasmas by modeling or experimental work for various processes to understand the inter-reliant dependency of plasma and packing materials [26, 30–34]. Butterworth et al. [35] found that a decrease in the particle size (180–2000 µm) of the packing (Al_2O_3 and $BaTiO_3$) significantly affected the discharge behavior of the plasma for CO_2 reduction, as surface discharging became increasingly dominant over micro-discharges due the increase of local contact points. In a subsequent study, Butterworth et al. [36] developed a single pellet reactor, investigating the effects of the dielectric constant (4–4000) on the co-dependency of the plasma and packing, across a wide range of applied voltages in an N_2 plasma. Results showed that the threshold of the observed discharge phenomena, partial and surface discharging, was dependent on the dielectric constant of the packing. Furthermore, the ignition properties of the plasma were found to vary, as materials with moderate/high dielectric constant tend to ignite as partial discharges, contrasting to materials with low dielectric constant where the ignition occurs directly in the surface streamer mode. Similar research efforts have been directed toward plasma-assisted NOCM. Results of earlier research dealing with plasma-assisted NOCM have primarily used packing materials, such as glass beads, glass wool, sea sand, γ-Al_2O_3, α-Al_2O_3, and $BaTiO_3$. Kim et al. [37] investigated the influence of the particle size (1–149 µm) and dielectric constant on NOCM in a DBD plasma, where the gap distance of the particles (KIT-6, sea sand, α-Al_2O_3) was found to be an influential parameter on the conversion and product composition. Outcomes of the study revealed an increase in the selectivity towards unsaturated C_2 species by decreasing the particle size of the packing, due to increased interactions between CH_4 and oxygen ion vacancy sites on the particles, facilitating the formation of methyl radicals and dehydrogenation routes of saturated C_2 species. Also, Taheraslani et al. [38] examined the effects of the dielectric properties and porosity of the packing ($BaTiO_3$, γ-Al_2O_3, α-Al_2O_3, Silica-SBA-15) on NOCM in a DBD plasma. The results showed an improved CH_4 conversion and C_2 yield using α-Al_2O_3 and γ-Al_2O_3 as the packing, whereas the performance of $BaTiO_3$ was observed to be poor, attributed to the small pores and high dielectric constant of $BaTiO_3$, impeding the enhancement of the local electric field.

As outlined, significant research efforts have been made to understand the co-dependent dynamics of combining NTP with packing materials. However, the underlying mechanisms are still far from understood. The scope of this work is related to the fundamental understanding of the packing materials' effect on plasma dynamics in a co-axial DBD and how this influences NOCM chemistry. Unlike other studies [37–39], the plasma-assisted NOCM was conducted using an undiluted CH_4 feed stream. For this purpose, inert glass beads of different sizes were utilized as packing in the DBD reactor. To understand and explain the observed changes in CH_4 conversion and the product composition, electrical characterization of Lissajous figures was used to elucidate and analyze the plasma behavior and discharge phenomena. In addition, the limitations of existing analysis techniques and equivalent circuit models is discussed. The major outcome of this study is related to the plasma and packing material dependency that was proven to significantly alter the NOCM chemistry in a co-axial DBD. A substantial increase in selectivity towards unsaturated C_2 was observed and was suggested to be an effect entirely related to changing plasma dynamics showing the importance of particle size on the plasma behavior.

Experimental Set-Up

Geometric Specifications and Operating Conditions of the DBD Plasma Setup

The NOCM experiments were conducted in a coaxial packed-bed DBD reactor. This DBD configuration consists of five main components: a customized cylindrical quartz glass reactor acting as the dielectric, two electrodes, and two end plugs, as shown in Fig. 1.

The cylindrical quartz glass reactor had inner and outer diameters of 19 mm and 22 mm, respectively, resulting in a dielectric barrier thickness of 1.5 mm. The outer electrode, working as the high voltage electrode, was a 5 cm long stainless steel mesh (wire diameter = 0.22 mm, mesh size = 415 μm) covering the outer surface area of the quartz glass reactor. The inner grounded electrode was a stainless steel rod with a diameter of 10 mm, fixed at the center of the tube, resulting in a gap distance of 4.5 mm. The high voltage electrode was powered by a Trek 20/20C-HS-H-CE high voltage amplifier, capable of giving voltage amplitudes of up to 20 kV peak alternating current at frequencies up to ~ 10 kHz. A Tektronix function generator (AFG1022) controlled the signal, selecting the frequency and

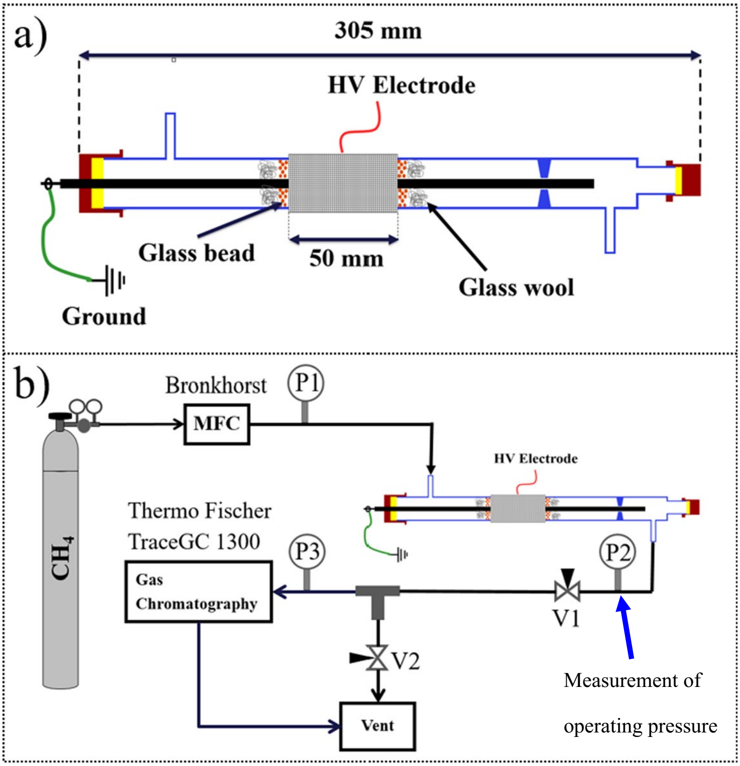

Fig. 1 **a** Schematic diagram of the applied packed bed DBD plasma reactor. The schematic drawing is color coded to distinguish the different materials: quartz glass reactor (blue), end plastic plugs (dark red), silicone O ring (yellow), stainless steel rod (black), stainless steel mesh (grey), glass beads (orange), insulated grounded wire (green), insulated HV cable (red). **b** Schematic representation of the experimental setup, showing the gas lines, position of manometers (P1–P3), needle valves (V1 and V2) and GC. The operating pressure in the reactor was measured using P2 located just after the reactor (Color figure online)

the peak-to-peak voltage to the Trek amplifier. The electrical characterization of the plasma was obtained by monitoring three electrical signals: the voltage output from the amplifier, the total current, and the charge transfer in the reactor. The voltage output from the Trek amplifier was measured using a Tektronix high-voltage probe (P6015A) connected to the outer HV electrode, whereas the total current was measured using a Rogowski coil (Pearson, 4100) installed on the grounded line. The charge transfer in the reactor was obtained by measuring the voltage across a ceramic monitor capacitor with a capacitance of 10 nF using a low-voltage probe (Picotech, TA150). A digital oscilloscope (Picotech, Picoscope 6402C) recorded and collected these signals for continuous measurements of the DC plasma power during the experiments that were conducted. The plasma power was determined by integrating both the instantaneous plasma power and the enclosed area of the resulting Q–V diagram for a number of cycles (8 cycles were used). These charge–voltage (Q–V) diagrams were continuously acquired and saved every 5 min during the experiment to elucidate the electrical properties of the plasma. A schematic representation of the experimental setup in terms of the applied diagnostics is presented in Fig. 2.

The plasma was generated in the DBD reactor by applying voltages of ~ 31–34 kV at a fixed frequency of 3 kHz, resulting in a plasma power of 30 W ± 1.5 W. Upon ignition, the reactor was flushed in CH_4 (Air liquid, N55, > 99.9995%) and a plasma stabilization period of 30 min at a plasma power of 30 W was practiced prior to any measurements. This was practiced to let the system equilibrate, heat the gas by the plasma, and ensure steady state operation during the experiments. The CH_4 gas was introduced to the inlet glass joint via

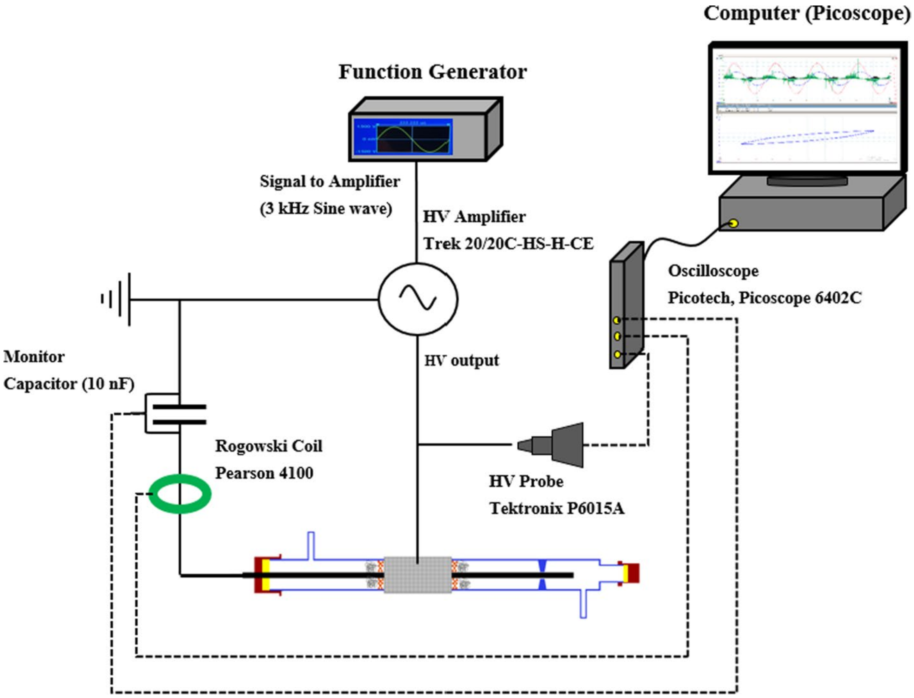

Fig. 2 Schematic diagram of the experimental setup showing the configuration and connections of the electrical circuit

silicone tubing at a volumetric flow rate of 50 Nml/min by Bronkhorst mass flow controllers. Noteworthy is that no dilution gas was used in any of the conducted experiments. Experiments were conducted at two different pressures, i.e., a low- and a high-pressure condition. The low-pressure tests constitute reaction conditions similar to ambient conditions ($p = 1.2$ bar), whereas the high-pressure tests correspond to a slightly elevated pressure ($p = 1.7$ bar). These operating pressures were kept at 1.2 bar and 1.7 bar and monitored during the experiments. The reactor pressure was monitored and regulated manually using a needle valve (V1) and a manometer (P2) placed right after the reactor outlet, as depicted in Fig. 1b. The product composition of the effluent gas stream was analyzed using an online gas chromatograph (Thermo Fischer TraceGC 1300). The GC was calibrated to measure the following species: N_2, CH_4, C_2H_2, C_2H_4, C_3H_6, C_3H_8, and C_4H_{10}. To account for the gas expansion of the outflow from the reactor, a small N_2 flow of 8 Nml/min was added to the reactor effluent as a standard for the GC measurements, allowing for estimation of the volumetric outflow. Before every experiment, the volumetric flow rate and inlet concentration of CH_4 was measured from at least three GC samplings. The peaks from the chromatograms were converted to concentrations using the calibrations, as they were integrated and averaged for the steady-state operation. Thus, the molar flow rate of the products and unreacted CH_4 was calculated from the volumetric outflow and the product concentrations from the GC measurements, allowing for conversion and selectivity calculations. Further, the standard deviation of the integrated peaks of the various species from the calibrations and experiments was determined and used to estimate the uncertainty on the concentration of every specie. The column that was installed in the GC was a RESTEK Rtx-5. The GC was also equipped with a flame ionization detector (FID) and a thermal conductivity detector (TCD), both using helium as carrier gas. The conducted experiments were repeated with a fresh packing of glass beads to account for uncertainties. All experiments were conducted without any external heating, and the duration of an experiment was 100 min, corresponding to five GC measurements of the continuous effluent gas stream. The operating conditions and relevant geometric specifications used in this study are summarized in Table 1.

Additional information regarding the experimental methodology (estimation of molar flows, GC specifications, reactor filling, photographic documentation (Figure S1) of the reactor with fresh and spent packing, estimation of packing density, residence time calculations,

Table 1 Overview of the geometric specifications and operating conditions used in this study

Geometric specifications	Value
Reactor inner diameter [mm]	19.0
Inner electrode diameter [mm]	10.0
Discharge gap [mm]	4.5
Outer electrode length [cm]	5.0
Plasma zone volume [cm^3]	10.3
Operating conditions	**Value**
Frequency [kHz]	3
Plasma power [W]	30
Volumetric flow rate, CH_4 [Nml/min]	50
Temperature	Ambient, no external heating
Low-pressure condition [bar]	1.2
High-pressure condition [bar]	1.7

and plasma power measurements (Figure S2)) is provided in section S.1 in the supplementary information (SI).

Packing Materials

The packing materials tested in this study were glass beads of five different size distributions, as listed in Table 2. The beads were tightly packed in the gap between the inner electrode and the glass barrier across the bed zone. Quartz glass wool was placed on each side of the bed zone, to restrict any movement of the glass beads elsewhere of the plasma zone. After the packing procedure for the glass beads and fixation with glass wool, the zone was slightly compressed, with a thin metal rod, to ensure the densest packing possible for the beads. It can be noted that the reactor porosity of the various sizes is quite similar, except for the largest particles with a size of the same order of magnitude as the gap distance, which hinders a tight packing. The procedure for estimation of the packing porosity of the different bead sizes is described in the SI in section S.1.

Evaluation Criteria: Conversion, Product Selectivity, and Energy Efficiency

The performance of the different plasma-glass bead systems was evaluated in terms of CH_4 conversion, product composition, and energy efficiency. The conversion of CH_4 (X) and selectivity (S) were obtained according to Eqs. (1) and (2), where (x) denotes the number of carbon atoms and (F) denotes molar flow rates in and out of the reactor of specific compounds in the unit mol/s.

$$X_{CH_4}(\%)=\frac{F_{in,CH_4}-F_{out,CH_4}}{F_{in,CH_4}}\cdot 100\% \tag{1}$$

$$S_{C_xH_y}(\%)=\frac{x\cdot F_{C_xH_y}}{F_{in,CH_4}-F_{out,CH_4}}\cdot 100\% \tag{2}$$

The carbon balance (CB) is defined according to Eq. (3), taking the ratio between the sum of the effluent carbon atoms of each product relative to the inlet number of carbon atoms. The CB was used as a control parameter to validate that the GC measurements covered all formed major species in the product stream.

Table 2 Overview of the different utilized bead sizes and their corresponding reactor porosity and dielectric constant

Bead size distribution [μm]	Packing porosity, V_{void}/V_{total}	Dielectric constant, ε_r	Sphericity, Ψ	Supplier
Glass beads				
2000–5000	0.75	4	≈ 1	Sigma Aldrich
900–1100	0.45	4	≈ 1	Assistent
425–600	0.41	4	≈ 1	Sigma Aldrich
212–300	0.41	4	≈ 1	Sigma Aldrich
150–212	0.36	4	≈ 1	Sigma Aldrich

$$\mathrm{CB}(\%)=\frac{\sum \mathrm{x}\cdot \mathrm{F}_{\mathrm{C_xH_y}}}{\mathrm{F}_{\mathrm{in,CH_4}}}\cdot 100\% \tag{3}$$

The energy efficiency (η) of the NOCM was defined in terms of the higher heating value (*HHV*) and calculated as the fraction of accessible energy of the products relative to the energy of the converted amount of CH_4 and the applied plasma power, as seen in Eq. (4). The molar flow of hydrogen (F_{H2}) in Eq. (4) is theoretically estimated from the CH_4 reactions shown in the SI in section S.1 due to the fact that helium was used as the carrier gas on the TCD in the GC, preventing a precise quantification of the hydrogen concentration.

$$\eta(\%)=\frac{\sum_{\mathrm{x}=2}^{\mathrm{x}=3}\mathrm{HHV}\left(\mathrm{C_xH_y}\right)\cdot \mathrm{F}_{\mathrm{C_xH_y}}+\mathrm{HHV}\left(\mathrm{H_2}\right)\cdot \mathrm{F}_{\mathrm{H_2}}}{\mathrm{HHV}\left(\mathrm{CH_4}\right)\cdot(\mathrm{F}_{\mathrm{in,CH_4}}-\mathrm{F}_{\mathrm{out,CH_4}})+\mathrm{Plasma\ power}}\cdot 100\% \tag{4}$$

Results and Discussion

This section provides a thorough evaluation of the tested plasma-glass bead systems in terms of CH_4 conversion, product composition, and energy efficiency. Further, electrical characterization of the plasma dynamics has been conducted to obtain a detailed analysis of Q–V plots (also known as Lissajous plots), illuminating the transition of discharge regimes obtained for the different bead sizes.

Conversion of CH_4, Product Composition, and Energy Efficiency

The obtained conversion of CH_4 and the energy efficiency for the high- (1.7 bar) and low-pressure (1.2 bar) conditions as a function of the bead size and a comparison to an empty reactor (blue dashed line, p = 1.2 bar) are provided in Fig. 3. Additional time on stream data for the conducted experiments is provided in the SI in Figures S3-S10.

The CH_4 conversion was found to be relatively low in contrast to other studies [37–39] and observed to decrease with decreasing bead sizes for both pressure conditions, as seen in Fig. 3a. The low CH_4 conversion is likely due to the absence of a dilution gas in the feed stream since the presence of a dilution gas (up to 90 vol% is commonly used) typically enhances the discharge homogeneity and conversion of CH_4 [40]. An undiluted feed was used since it is much more industrially relevant, allowing for easier separation of products from unconverted feed. Similarly to the CH_4 conversion, the same tendency is reflected in Fig. 3b, showing a decreasing energy efficiency for the plasma-assisted NOCM with decreasing particle size. This is a result of the low conversion of CH_4 and constant plasma power of 30 W, yielding low energy efficiencies. The effect is more prominent for the high-pressure condition, as the CH_4 conversion decreased from 8.5 to 3.7%, compared to the low-pressure condition, where the CH_4 conversion only decreased from 8.7 to 5.5%. Comparing the CH_4 conversion of the two pressure conditions for the two largest applied glass beads (2000–5000 µm and 900–1100 µm), almost identical reactor performances are observed. Due to the higher porosity of the large particle packing, the residence time of the gas is longer than for the next largest bead size (2000–5000 µm vs 900–1100 µm), indicating increases in residence time caused by the different bead sizes seems not to improve the conversion

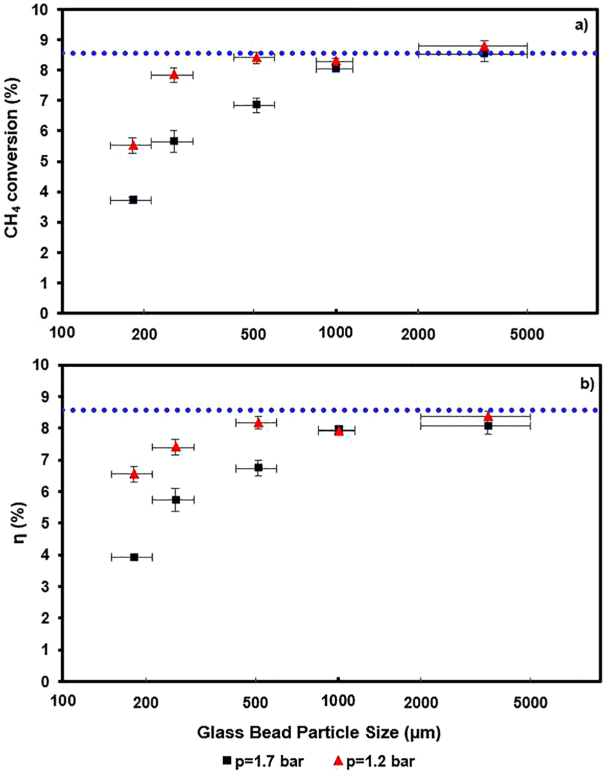

Fig. 3 **a** CH_4 conversion and **b** energy efficiency, as a function of the particle size of the glass beads. Results from an empty reactor (1.2 bar) experiment is also shown for comparison. Horizontal and vertical error bars indicate the span of the bead size and the standard deviation of the four last GC measurements. The operating conditions and geometric specifications of the investigated plasma systems can be found in Table 1

result. Furthermore, an identical CH_4 conversion is obtained for the empty reactor exhibiting the longest gas residence time. Thus, the CH_4 conversion dependency on particle size, more prominently observed for the high-pressure condition, may be a combined effect of the slightly elevated operating pressure (1.7 bar) and spatial confinement of the plasma zone and its impact on the plasma. The observed effect appears to become increasingly important with decreasing size of the interparticle void spaces. To substantiate this, Fig. 4, shows the CH_4 conversion as a function of either the gas residence time or number of micro-discharges per half cycle. The results shown in Fig. 4a indicate that the CH_4 conversion is roughly independent of the gas residence time between 5 to 12 s and 8 s to 13 s for the low- and high-pressure conditions, respectively.

For shorter residence times < 5.5 s and < 7.8 s for the low- and high-pressure conditions, the decrease in CH_4 conversion shown in Fig. 4a may be a combined effect of transitional plasma dynamics affected by decreasing bead size and the residence time decrease (caused by the different bead sizes). However, the transitional plasma dynamics are anticipated to play a relatively larger role due to the fact that the residence time for the three smallest bead sizes is very similar, as shown in Table 3. In addition, as seen in Fig. 4b, the

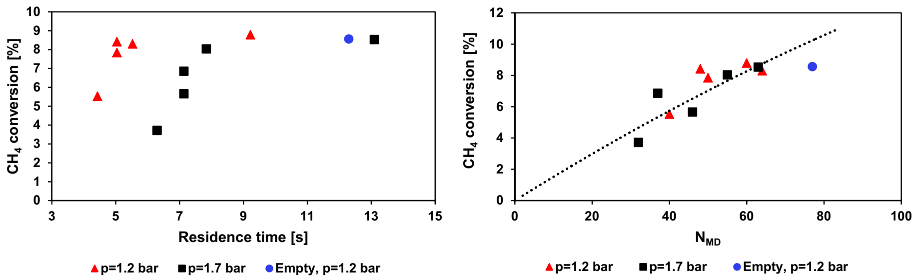

Fig. 4 **a** CH_4 conversion as a function of the gas residence time for the two different pressure conditions. **b** CH_4 conversion as a function of the number of micro-discharges pr. half cycle (N_{MD}). N_{MD} was determined by examining the current profile according to the method of Andersen et al. [41]

CH_4 conversion is correlated with the plasma mode and, more specifically, the number of micro-discharges formed in the reactor. The number of micro-discharges was estimated by examining the current profiles which are shown later in "Electrical Characterization of Resulting Plasma Dynamics" section. To elaborate, an algorithm was used to count the micro-discharges and if the current spikes or peaks increase above the standard deviation, similar to the study of Andersen et al. [41]. A thorough discussion of the transitional plasma dynamics for the different bead sizes is provided in "Electrical Characterization: Theory and Methodology" section. Furthermore, a comparison of the residence times and number of micro-discharges for the different beads sizes is shown in Table 3.

The results presented in Fig. 5 demonstrate that not only is the CH_4 conversion affected by the different applied glass bead sizes, but also the resulting product compositions and carbon balances for both pressure conditions. The main products obtained for the two pressure conditions consisted of a mixture of saturated and unsaturated C_2 and C_3 species, as shown in Fig. 5a. The exact degree of saturation between saturated and unsaturated C_2 and C_3 was not determined due to separation limitations of the RESTEK Rtx-5 column utilized in the GC, which we are aware is not ideal. Preferably, another GC column should have been used to allow for this determination of the saturation degree between unsaturated C_2. However, based on results from a similar study [40], it is expected that ethylene constitutes an equivalent or slightly larger fraction than acetylene of the measured unsaturated C_2 species. In addition to the main products summarized in Fig. 5a, longer hydrocarbon products were detected (C_4 and C_5) in

Table 3 Comparison of the residence time and number of micro-discharges per half cycle for the different bead sizes and operating pressures

Glass bead distribution, [µm]	Residence time (τ) [s]		Number of micro-discharges per half cycle (N_{MD})	
	p = 1.7 bar	p = 1.2 bar	p = 1.7 bar	p = 1.2 bar
150–212	6.27	4.43	32	40
212–300	7.14	5.04	46	50
425–600	7.14	5.04	37	48
900–1100	7.84	5.53	55	64
2000–5000	13.1	9.22	63	60
Empty	–	12.3	–	77

Fig. 5 **a** Carbon selectivity of the products in the effluent stream for the high- and low-pressure conditions (as indicated on the figure) and for the different glass bead sizes. Note the empty reactor results are shown combined with the low-pressure condition. **b** Resulting carbon balance of the different tested glass bead sizes for the two pressure conditions

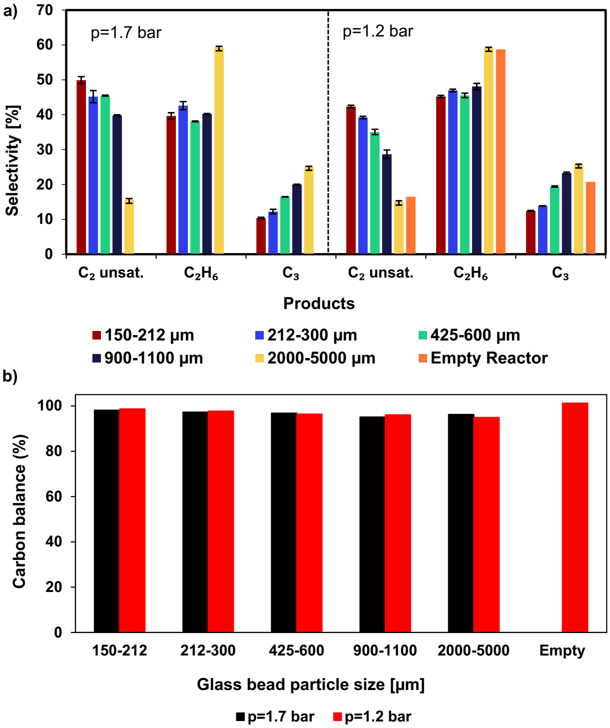

the FID spectrum, however, the concentrations (trace amounts) were insignificantly low, and were not accounted for. Therefore, these longer hydrocarbons were neglected in the calculation of the carbon selectivity of the different products, which is a reasonable approach, substantiated by the carbon balances shown in Fig. 5b, covering > 95% of the fed carbon for both pressure conditions. However, it should be mentioned that the good closure of the carbon balances is partly due to the low conversion of CH_4. Furthermore, the carbon balance closure decreases slightly with larger bead size, which could be a result of formation of higher hydrocarbons or carbon deposition on the beads. Whether the latter has a significant influence on the carbon balance or conversion of CH_4 longer experiments would have to be conducted and the amount of deposited carbon quantified.

The results presented in Fig. 5a show a significant increase in selectivity towards unsaturated C_2 species with decreasing bead size for the investigated high- and low-pressure conditions, from 16 to 50% and 15 to 42% for the high- and low-pressure conditions. Also noteworthy is that the empty reactor and the largest bead size showed very similar product selectivities. The most prominent increases in selectivity towards unsaturated C_2 are observed when comparing the largest bead size (2000–5000 µm) and empty reactor with the second largest bead size (900–1100 µm). The highest selectivity towards unsaturated C_2 species for the high- and low-pressure conditions was 50% and 42%, respectively. Furthermore, it should be noted that the high-pressure condition, except for the largest bead size (2000–5000 µm), consistently enhances the selectivity towards unsaturated C_2 species relative to the selectivity towards the saturated C_2H_6 compared to the low-pressure condition.

In contrast, the selectivity towards saturated C_2 (ethane) remained approximately constant with bead size, whereas the selectivity towards C_3 species decreased with decreasing bead size for both pressures. This indicates that the activation mechanism of CH_4 and the dominating reaction routes determining the chemistry of NOCM are affected by the applied size of the glass beads. From the results shown in Fig. 5a, and in line with other studies proposing various reaction paths [40, 42], it is proposed that the formation of C_3 species most likely proceeds through an activation mechanism of unsaturated C_2 with CH_x species (R1) or hydrogen radicals (R2) or electron impact dehydrogenation of C_2H_6 (R3 and R4). With decreasing bead size, the reaction pathways (R1 and R2) appear to be progressively inhibited, favoring the formation of unsaturated C_2 rather than C_3 species via these reaction pathways.

$$C_2H_4 + CH_2 \rightarrow C_3H_6 \tag{R1}$$

$$C_2H_4 + H \rightarrow C_2H_5 \tag{R2}$$

$$C_2H_6 + e^- \rightarrow C_2H_5 + H + e^- \tag{R3}$$

$$C_2H_5 + CH_3 \rightarrow C_3H_8 \tag{R4}$$

The change in product selectivity is suggested to be primarily an effect of changing streamer dynamics related to the co-dependent behavior of the plasma and the packing beads rather than a gas residence time or CH_4 conversion effect. This is substantiated in Fig. 6, which displays the selectivity to unsaturated C_2 as a function of the number of micro-discharges per half cycle. Following these results, the selectivity towards unsaturated C_2 is found to be correlated with the number of micro-discharges in the DBD reactor and, thereby, the dominating plasma regime.

The overall reactor performance of the conducted plasma-assisted NOCM for the empty reactor and utilizing glass beads of the five different bead sizes is summarized in Fig. 7. The results show the selectivity towards unsaturated C_2 plotted against the CH_4 conversion for the two pressure conditions. The results in Fig. 7 emphasize that the optimal reactor configuration depends on whether the purpose is conversion or selectivity to unsaturated products. A high selectivity towards unsaturated C_2 species is not directly correlated with the highest CH_4 conversion, as seen from the results utilizing the largest glass beads (2000–5000 µm) and vice versa. As demonstrated, the intermediate glass bead sizes

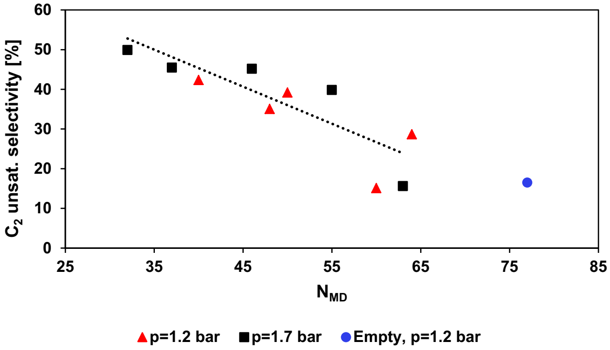

Fig. 6 CH_4 conversion as a function of the number of micro-discharges per half cycle

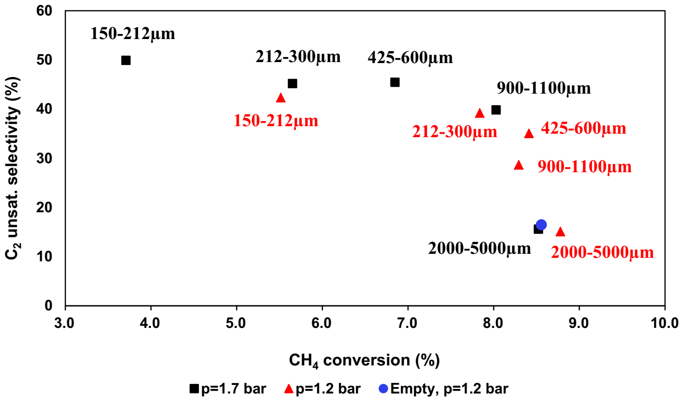

Fig. 7 Carbon selectivity to unsaturated C_2 species plotted against the conversion of CH_4

(212–300 µm, 425–600 µm, 900–1100 µm) contribute to a higher conversion of CH_4 while simultaneously being selective towards unsaturated C_2 species, exhibiting the most optimal reactor performance for the plasma-assisted NOCM. This characteristic reactor performance for the different tested glass bead systems is, however, not captured by the energy efficiency factor provided in Fig. 3b, as the performance of the sizes of the glass beads (425–600 µm, 900–1100 µm, 2000–5000 µm) displays similar performances. The results in this section show that the occurring chemistry in the plasma-assisted NOCM strongly depends on the size of the utilized glass beads. The change in reactor performance is attributed to the resulting plasma dynamics, i.e., the change of discharge regime and electron energies, which seems to be strongly dependent on spatial confinement and operating pressure. Understanding the transitional behavior of the discharge regime and streamer propagation related to operating conditions and the co-dependency of the packing material is very important and suggested to be the determining factor controlling the chemical reaction routes. This is discussed further in “Electrical Characterization: Theory and Methodology”–“Effects of Transitional Plasma Dynamics on the Chemistry of NOCM” sections, elucidating the relationship between the observed plasma dynamics, discharge regimes, and shapes of Q–V plots obtained for the different bead sizes.

Electrical Characterization: Theory and Methodology

Electrical characterization of reactor properties in PBR DBD plasmas is useful for exploring the inherently complex character of the co-dependent behavior of discharge regimes and the utilized packing material. For this purpose, the most commonly applied and, generally, the most accurate method is the capacitor method, also used in this study, as shown in Fig. 2. This allows for power measurements (by integrating the Lissajous figure with respect to time) alongside in-depth electrical characterization by analysis of charge–voltage (Q–V) plots, combined with a suitable equivalent circuit model, as shown in Fig. 8 [35].

As presented in Fig. 8, the simplest equivalent circuit model of DBD systems is often used to interpret ideal Q–V data by two capacitors in series, corresponding to the dielectric and gap capacitances (C_{diel} and C_{gap}) with a resistor (R_{plasma}), typically time-dependent, parallel to the gap capacitance to account for the variable conductivity of the gas gap

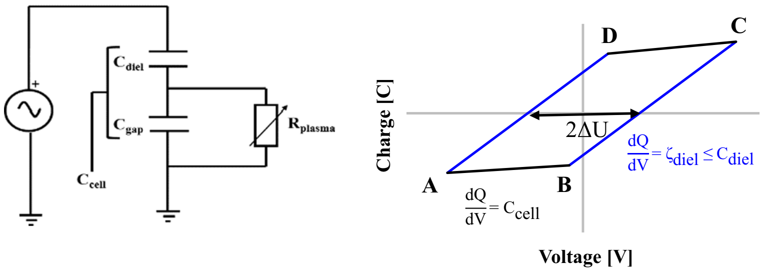

Fig. 8 Depiction of the equivalent circuit model of a classical DBD plasma based on series capacitances for the discharge gap and dielectric material, with a corresponding ideal Q–V plot shaped as a parallelogram for one cycle of the applied voltage. The color-coding corresponds to the capacitive phases (black) and the discharging phases (blue) of a classical DBD plasma (Color figure online)

during the discharge phase [35]. The ideal Q–V diagram for a sinusoidal voltage cycle of a DBD has the characteristic shape of a parallelogram with clearly distinguishable discharging phases. The four sides constitute a complete cycle of the applied voltage in a DBD. The discharge properties are derived from the gradient of the capacitive (AB and CD lines, 'plasma off') and discharging phases (BC and DA lines, 'plasma on'). During the 'plasma off' phase, the reactor works entirely as a capacitor with a capacitance equal to C_{cell} when no plasma is present. Conversely, during the discharging phase, the gas gap voltage exceeds the threshold breakdown voltage, generating micro-discharges that transfer charge across the gas gap in the DBD. Consequently, the gas gap ceases to behave as a capacitor, while the dielectric barrier remains capacitive, meaning the capacitance is equal to C_{diel} during the discharging phase. The capacitance of the dielectric, C_{diel}, is often a fixed value, neglecting temperature effects, and is only dependent on the reactor geometry and material properties. The relationship between the capacitances of the equivalent circuit model of DBDs is provided in Eq. 5. Further, the parameter ζ_{diel}, appearing in Fig. 8, corresponds to the effective dielectric capacitance, which is defined later in this paragraph.

$$\frac{1}{C_{cell}}=\frac{1}{C_{diel}}+\frac{1}{C_{gap}} \tag{5}$$

The Q–V plots combined with the equivalent circuit model are increasingly utilized as a diagnostic tool for power measurements and measurements of the gas gap charge transfer, reactor capacitance, and ignition voltage of the plasma. These are parameters that collectively quantify the reactor performance of the PBR DBD [35, 43, 44]. However, the dielectric properties of the packing material are known to enhance local electric fields in the vicinity of the bead or pellet, affecting the behavior of the plasma by effects of their polarization ability, often resulting in irregular forms of the Q–V plots [25, 35, 36]. A common irregularity observed and reported by previous studies [35, 36, 38, 45], exemplifying deviations from the ideal Q–V diagrams for PBR DBDs, is the occurrence of almond-shaped Q–V plots. The co-dependent dynamics of plasma and packing materials increase the complexity of interpreting the electrical behavior through analysis of almond-shaped Q–V plots of such systems as the capacitance during the discharging phases varies. Therefore, the transition point between the capacitive and discharging phases becomes undistinguishable, as the reactor capacitance during discharging varies due to the strong dependency on the externally applied voltage and capacitive properties of the packing [46]. Consequently, the description of the electrical behavior of PBR DBDs exceeds the application limitations of the classical equivalent circuit model. For this reason, the partial discharging formalism proposed by Peeters et al. [46], combined with extended methods of this theory by Butterworth et al. [36], have been used in this study to analyze the non-ideal Q–V plots. Hence, explaining the electrical behavior of the plasma in the tested PBR DBD systems for NOCM. The model of Peeters et al. [46] is an extension of the classical equivalent circuit model of DBDs, as seen in Fig. 9a, which accounts for the phenomenon of partial discharging by splitting the equivalent circuit geometry into two parts. One part describing the areal fraction of the non-discharging (α) and another part describing the discharging (β) areas of the electrode.

Partial discharge regimes are established in PBR DBDs, when the applied voltage only marginally exceeds the breakdown voltage of the reactor [35, 36, 47]. Under such conditions, if determinable, the discharging gradients (slopes BC and DA) would be less than the capacitance of the dielectric, C_{diel}, introducing the parameter, ζ_{diel}, termed as the effective capacitance, as shown in Fig. 8. However, the often irregular Q–V shaping implies difficulties with the determination of the effective capacitance. Thus, the extended methods of Butterworth et al. [36], based on the formalism of Peeters et al. [46], have been applied for this purpose, allowing for the electrical characterization of non-ideal Q–V diagrams for PBR DBDs. The analytical method characterizes the plasma behavior and dominating discharge regime in terms of the fractional area of the electrode that is non-discharging (α). Thereby, indirectly accounting for the variable gradient during the discharging phases through the determination of the effective capacitance. The partial discharge coefficient, α, is defined according to Eq. 6.

$$\alpha = \frac{C_{diel} - \zeta_{diel}}{C_{diel} - C_{cell}} \tag{6}$$

The value of α is defined in the range between zero and one and can be used as a qualitative measure to describe the plasma behavior and dominating discharge regime. In this respect, a low α value (~0–0.1) corresponds to an operating mode where almost complete charge transfer occurs, unaffected by the capacitive properties of the packing, represented

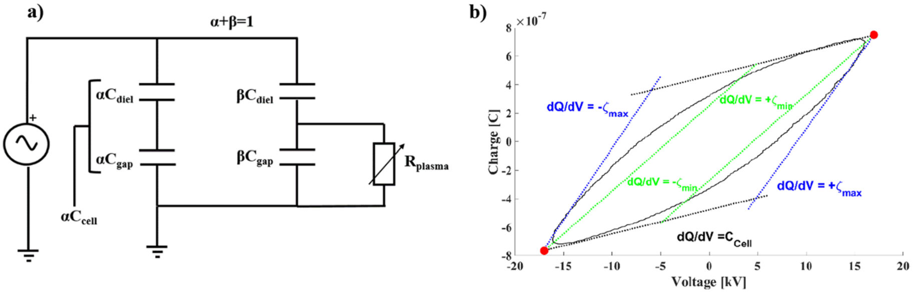

Fig. 9 **a** Depiction of the partial discharging equivalent circuit model proposed by Peeters et al. [46]. As shown, the dielectric and gap capacitances are divided into a non-discharging areal fraction (α), and a discharging areal fraction (β). **b** Visual representation of the application of the analytical approach proposed by Butterworth et al. [36] used to estimate the effective dielectric capacitance (ζ_{diel}). The estimation of the maximum and minimum effective capacitances for the positive and negative half cycles are based on the average of four consecutive AC cycles. This procedure has been repeated five times, every 20 min, to cover the full operating time and capture any transitional behavior of the resulting plasma. The data provided is from the experiment utilizing the glass bead size (212–300 μm) for the low-pressure condition

through a discharge regime of stable streamers bridging the discharge gap. Oppositely, a high alpha value (~ 0.9–1) is characteristic of incomplete plasma formation dominated by a partial discharging regime, limiting charge transfer across the discharge gap, as every single packing bead or pellet acts as individual capacitors. The controlling mechanisms of the transitional behavior of discharge regimes and streamer dynamics is a combined effect of the dielectric constant of the packing material and applied voltage. In practical applications of PBR DBD systems, the discharge dynamics are inevitably affected by the packing's capacitive ability, resulting in a varying instantaneous capacitance during the discharging phase, causing non-ideal forms of the Q–V diagram. To overcome analysis implications of irregular Q–V plots, the effective capacitance is measured four times during a full cycle of the applied voltage, defining a range of values for the effective capacitance. A visual depiction of the concept is provided in Fig. 9b. According to the analysis, the effective capacitance is determined through two sets of gradients, the maximum, and minimum, during the positive and negative half periods ($+\zeta_{\mathrm{diel,min/max}}, -\zeta_{\mathrm{diel,min/max}}$) of the full cycle. The maximum effective capacitance, ζ_{max}, corresponds to the steepest gradient of the discharging phases, whereas the minimum effective capacitance, ζ_{min}, corresponds to the gradient obtained between the apex points and the approximated beginning of the discharging phases. These gradients, the maximum and minimum effective capacitances ($+\zeta_{\mathrm{diel,min/max}}, -\zeta_{\mathrm{diel,min/max}}$) for the positive and negative half cycle, were estimated using linear regression based on a weighted least square method on four consecutive Q–V cycles. This procedure was repeated every 20 min to account for the possibility of changing plasma dynamics during the operation of the PBR DBD. Thereby, a span of values is averaged for the effective capacitance. The application of this concept is similar to the classical equivalent circuit model of DBDs, however, it allows for more accurate electrical characterization of non-ideal Q–V diagrams due to the estimation of the maximum and minimum effective capacitances. Deviations from ideality are related to the width of the interval range of the effective capacitances, as a difference of zero between the maximum and minimum value of the same half period would correspond to a constant gradient of C_{diel}, yielding an ideal parallelogram-shaped Q–V plot. The approach presented here and visually shown in Fig. 9b has been used for the characterization of the electrical behavior of the resulting plasma dynamics of the NOCM for the different glass bead systems. The parameter, α, has been calculated according to Eq. 6, requiring the effective capacitance, ζ_{diel}, the cell capacitance, C_{cell}, and the dielectric capacitance, C_{diel}, to be known. The effective capacitance, ζ_{diel}, and the cell capacitance, C_{cell}, are determined through analysis of the gradients according to Fig. 9b. Conversely, the dielectric capacitance, C_{diel}, is very often a fixed value solely dependent on geometry and material properties, as seen in Eq. 7 [48]:

$$C_{\mathrm{diel}} = \frac{2\pi\varepsilon_0\varepsilon_{\mathrm{r}}\mathrm{L}}{\ln\left(\frac{\mathrm{R+x}}{\mathrm{R}}\right)} \tag{7}$$

where ε_0 and ε_{r} are the absolute and relative permittivity of vacuum and quartz glass, respectively, and R, x, and L correspond to the reactor's inner radius, barrier thickness, and plasma zone length. By inserting the real dimensional values, a dielectric capacitance, C_{diel}, of ~ 71 pF for the reactor used in this study is obtained. The calculation is shown in the SI in Equation (S.10).

Electrical Characterization of Resulting Plasma Dynamics

The obtained Q–V plots for all the tested glass bead systems for both pressure conditions, alongside corresponding values of alpha, are provided in Fig. 10, clearly displaying non-ideal behavior. The Q–V plots presented in Fig. 10a, b demonstrate that a transitional behavior of the plasma with decreasing bead size occurs for both pressure conditions due to the shape transition. Similar electrical characterizations were observed for the plasma behaviors for the two pressure conditions. Therefore, the remaining part of this section is focused on elucidating the plasma behavior through the results obtained for the high-pressure condition, whereas the results showing the electrical data for the low-pressure condition are provided in Figure S11-S12 in the (SI). As seen in Fig. 10a, b, the shape of the Q–V plots shifts from an approximately characteristic parallelogram towards an elongated almond shape for decreasing bead sizes, featuring the distinct curved transition between the capacitive and discharging phases. The shift in shape is most distinctively observed when comparing the largest beads (2000–5000 µm) and the empty reactor with the remaining bead sizes. This plasma transition is also reflected and substantiated by the corresponding values of α provided in Fig. 10c. The α value is determined four times for a full cycle of the applied voltage due to its dependency on the effective capacitance, according to Eq. 6. For this reason, in Fig. 10c, the alpha coefficient is presented as a defined range of values, with the upper and lower boundary corresponding to the estimation acquired using the minimum and maximum gradient of ζ_{diel} for the positive and negative half cycle, as outlined in "Electrical Characterization: Theory and Methodology" section. The alpha value following the analytical methods of Butterworth et al. [36] can be interpreted as a measure of the fractional charge conductively transferred across the discharge gap between the electrodes. For increasing alpha values ($1 \geq \alpha \geq 0$), the packing material increasingly

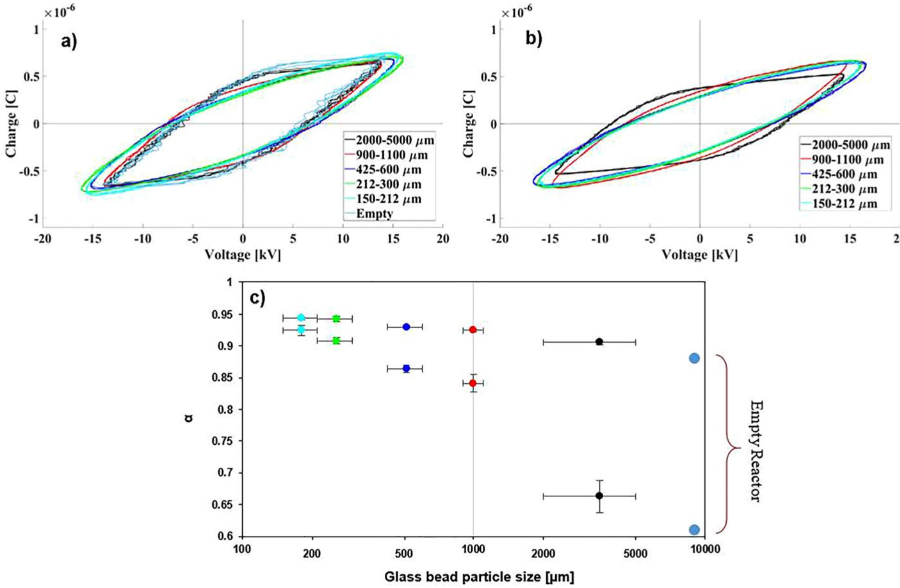

Fig. 10 Q–V plots measured for the different bead sizes (empty reactor, 150–212 µm, 212–300 µm, 425–600 µm, 900–1100 µm, 2000–5000 µm) for **a** the low (1.2 bar) and **b** high-pressure (1.7 bar) condition. **c** Estimated interval ranges for resulting α value for the high-pressure condition (p = 1.7 bar)

acts as a capacitor, limiting the charge transfer between the electrodes. In this respect, the value of α can be used as a measure reflecting the extent of plasma formation and the resulting discharge dynamics, wherein low alpha values correspond to a stable streamer regime, whereas a high value would correspond to partial discharging, as explained above. Previous studies have reported values of alpha in the intermediate range ($\alpha \sim 0.4–0.6$), and in such cases, the resulting plasma behavior was strongly dependent on the dielectric constant of the packing [36, 47]. In this respect, identical values of alpha and plasma powers can be obtained for different packing materials utilizing similar operating conditions, although significant differences in the discharge regime are observed. However, in this work, since the only tested packing material has been glass beads with an identical dielectric constant, the alpha estimations are considered a reliable parameter for characterizing the plasma behavior for the applied size relative to each other. In Fig. 10c, the determined values of alpha for the high-pressure condition are shown as an interval range. It is demonstrated that the width of the interval range of the alpha coefficient decreases towards a very narrow interval range in the high end of the spectra with decreasing bead size ($\alpha_{2000–5000\ \mu m} \sim 0.62–0.91$ to $\alpha_{150–212\ \mu m} \sim 0.92–0.95$) indicating that transitional plasma dynamics is obtained. The widest interval range for alpha alongside the lowest values is obtained for the largest glass beads (2000–5000 μm) and the empty reactor. This implies that the plasma behavior is characterized by a discharge regime where streamers appear, only partly affected by the capacitive properties of the glass beads, conductively transferring significant charge across the gas gap during discharging. The formation and propagation of intense streamers are suggested to be a result of the relatively high reactor porosity and large interparticle void spaces creating physically unhindered gap channels, facilitating the possibility of initiating breakdown in these gas channels. Thereby, bridging streamers appear, transferring significant charge, which is confirmed by the stepped discharging regions of the Q–V plots in Fig. 10a, b, which are found to be more prominent for the low-pressure condition [35, 36]. On the other hand, for the glass bead sizes smaller than the largest (900–1100 μm to 150–212 μm), the plasma zone becomes more spatially confined, referring to Table 2, substantially affecting the alpha coefficient, suggesting transitioning behavior of the plasma and dominating discharge regime. The decreasing glass bead size lowers the reactor porosity, which increases the gap capacitance of the reactor due to the increasing amount of glass beads present in the bed. Further, the interparticle void spaces decrease, which reduces the possibility of having radial physically unhindered channels through the packed bed, restricting the occurrence of bridging streamers. As a result, the interval range of alpha is observed to be consistently narrow ($\alpha_{900–1100\ \mu m} \sim 0.83–0.93$ to $\alpha_{150–212\ \mu m} \sim 0.92–0.95$), as shown in Fig. 10c, indicating that the combined effect of the lower reactor porosity and increasing zone capacitance affect the plasma formation and propagation. This limits the charge transfer during discharging, as every bead acts as individual capacitors by trapping charge. Consequently, the increasing alpha values suggest that the discharge regime transitionally shifts toward a regime dominated by partial discharging, absenting stable streamers bridging the discharge gap. This causes incomplete plasma formation and restricts charge transfer during discharging, resulting in almond-shaped Q–V plots. These inter-reliant plasma and packing mechanisms, experimentally demonstrated in this study, are designated to control the discharge dynamics and, thus, the electron energy distribution and densities that directly influence the chemical reaction routes [36, 46]. The assessment of these effects, related to the changing plasma regime and to which extent the NOCM is dependent on these dynamics, are addressed and clarified in "Effects of Transitional Plasma Dynamics on the Chemistry of NOCM" section.

The varying spatial confinement of the bed associated with the different sizes of the glass beads is also suggested to influence the ignition characteristics of the plasma. The origin of the complicated plasma behavior of partial discharge regimes has previously been stated to be related to the ignition mechanism of the plasma, which is dependent on the polarization ability and capacitive properties of the packing materials [35, 36]. During an AC voltage cycle, not necessarily in the peak, the gap voltage exceeds the threshold breakdown voltage in the contact points of the packing material due to enhanced local electric fields, igniting the plasma. With increasing AC voltage, as long as the breakdown criteria are fulfilled, the plasma propagates radially away from the ignition point, on a timescale of nanoseconds, conductively transferring charge towards nearby regions with larger discharge gaps and thereby weaker electric fields. These radially varying expansion conditions for the plasma constitute the complex behavior of partial discharging regimes associated with PBR DBDs, resulting in the varying discharge gradient alongside altering breakdown voltage and almond-shaped form of the Q–V plot. Figure 10a, b show that the discharging regions of the Q–V plots for the largest glass bead (2000–5000 μm) are slightly more defined and distinguishable. In contrast, the remaining four glass bead sizes feature the curved transition between the capacitive and discharging phases, exhibiting the non-ideal almond-shaped Q–V diagrams. Alone, the observed shape transition of the Q–V diagrams substantiates the changing character of the plasma with varying reactor porosity. The distinctive difference in the discharging regions of the Q–V plots further suggests that the ignition mechanism occurs differently and is strongly influenced by the reactor porosity. As outlined previously, the volume of the interparticle void spaces changes significantly with the interval range of the applied bead sizes. Herein, the increasing density of contact points for the smaller glass beads combined with the absence of physically unhindered gap channels suggests ignition in the contact point due to electric field magnification effects. Oppositely, the stepped profile of the discharging phases of Q–V plots for the empty reactor and largest glass beads (2000–5000 μm) suggests that the plasma ignition and breakdown mechanism proceeds through streamers. In addition to the Q–V plots and alpha coefficients presented in Fig. 10, the voltage and instantaneous current data, shown in Fig. 11, provide additional insight into the plasma behavior that substantiates the distinctive transition of the discharge dynamics with decreasing particle size.

The most apparent characteristic in Fig. 11 is the difference in the magnitude of the instantaneous current pulses. The empty reactor and the largest glass beads (2000–5000 μm) exhibit significantly higher current pulses than the rest of the tested glass bead sizes. This validates that the discharge regime is established by the formation and propagation of streamers. Moreover, a shorter discharging period is observed for the largest glass beads (2000–5000 μm), comprising a filament distribution of relatively intense current pulses for both the negative and positive half cycles, demonstrating symmetrical discharging. The shorter discharging duration indicates that a higher breakdown voltage is required to initiate the breakdown mechanism. This is attributed to the greater reactor porosity, wherein the plasma zone is less spatially confined, resulting in fewer contact points that would have increased the existence of narrow channels, allowing the breakdown mechanism to progress through streamers due to the weaker electric field magnification effects. Oppositely, considering the remaining four glass bead sizes, the discharging duration, filament distribution, and discharging symmetry are observed to change with decreasing bead size, with the specific bead size (900–1100 μm) exhibiting transitional behavior. Irrespective of the relatively high values of α estimated for this bead size (900–1100 μm), high-magnitude current pulses intermittently occur during discharging, indicating that the plasma behavior is found in an alternating state, transitioning between the propagation of

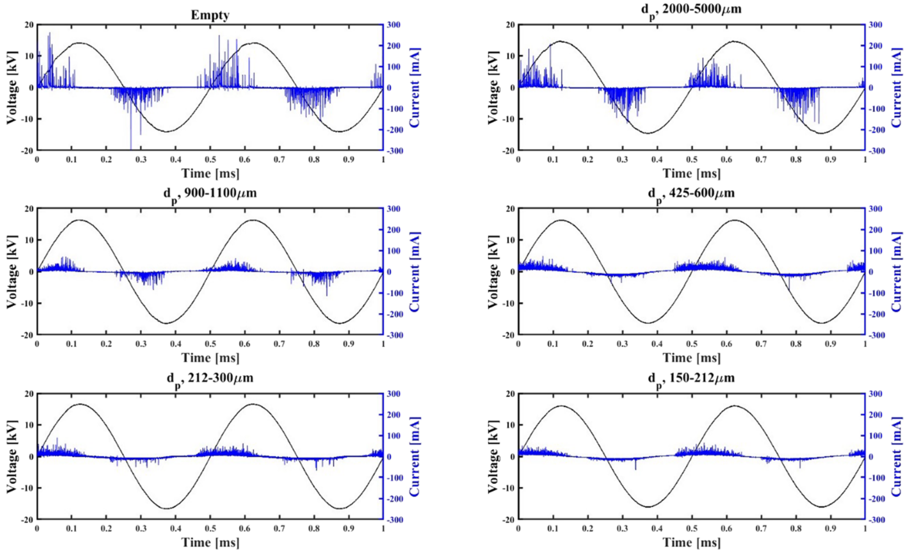

Fig. 11 Voltage-current characteristics for the empty reactor (1.2 bar) and tested glass bead systems measured after 40 min run time for the high-pressure condition. The presented discharge characteristics was filtered with a 20-point Savitzky–Golay filter to minimize noise (Color figure online)

streamers and partial discharging regimes. A magnification of voltage-current characteristics for the three smallest glass bead sizes (425–600 µm, 212–300 µm, 150–212 µm) is shown in Figure S13 in the SI. Marginal increases in the discharging duration are observed with decreasing particle size, indicating that the increasing spatial confinement of the bed contributes to a reduction of the breakdown voltage, substantiating that the ignition occurs in the contact points of the glass beads, resulting in uniform filament distribution. Further, with decreasing particle size of the glass beads, most prominently displayed for the smallest glass beads (150–212 µm), an increasing tendency to asymmetrical discharging is observed, implying that varying plasma behavior for the positive and negative half cycles of the applied voltage is obtained. This phenomenon may be attributed to a combined effect, which develops with increasing spatial confinement of the plasma bed and the inherent asymmetric reactor design with only one of the electrodes being covered with a dielectric [35]. The results presented in this section demonstrate that the plasma behavior, given the constant operating conditions aiming to yield a plasma power of 30 W, strongly depends on the discharge zone's capacitance, which is collectively defined by the physical properties of the packing material and the gas. This dependency was demonstrated by varying the bead size of the packing rather than the dielectric constant. The increasing spatial confinement of the bed substantially changed the character of the plasma, as the partial discharging degree was proven to increase and become the dominating discharge regime. This effect of the glass beads on the plasma behavior inevitably affects the charge transfer between the electrodes, which, together with the breakdown criterion, determines excitation, dissociation, and ionization rates that collectively influence the chemical reaction routes of the plasma-assisted NOCM [46].

Effects of Transitional Plasma Dynamics on the Chemistry of NOCM

As demonstrated in this study, through analysis of Q–V plots and voltage-current characteristics, a transitional behavior of the dominating discharge regime is observed. A transition from a streamer regime to a partial discharging regime, with increasing spatial confinement of the plasma zone is observed to occur. However, the important question to address is how the chemistry of NOCM is affected by the change in plasma dynamics.

The Conversion of CH_4

The results provided in "Conversion of CH4, Product Composition, and Energy Efficiency" section showed a correlation between the plasma behavior for the different bead sizes and the CH_4 conversion. In Fig. 4b, it was shown how the resulting plasma dynamics, in particular how the increasing number of micro-discharges was correlated with an increasing conversion of CH_4. Further, the results in Fig. 4a indicated that the gas residence time reduction caused by the glass beads did not influence the CH_4 conversion for large bead sizes. When the gas residence time is increased roughly by a factor of two, when going from the largest beads to the empty reactor, the CH_4 conversion remains constant at both pressures. This is substantiated for the three smallest bead sizes (150–212 µm, 212–300 µm, 425–600 µm), as the low-pressure condition, despite the shorter residence time compared to the high-pressure condition, demonstrated a higher CH_4 conversion. Thus, the results suggest that it is primarily a plasma effect related to the shift in discharge regime rather than a residence time effect that causes changes in the CH_4 conversion, however, for small beads an effect of residence time cannot be excluded.

Herein, two influential characteristics should be highlighted. Firstly, the formation and propagation of bridging streamers between the electrodes for the largest beads increase the probability of activating the strong CH_3-H bonds (~439 kJ/kmol) of CH_4, enhancing the conversion [49]. Secondly, the lower magnitude of current pulses alongside the asymmetric discharge dynamics, observed in Fig. 11, with the decreasing size of the beads, is anticipated to diminish the activation and, in turn, the conversion of CH_4.

Despite very similar plasma behaviors and characteristics for the two pressure conditions for the applied bead sizes, a difference in CH_4 conversion is observed when comparing the three smallest bead sizes (150–212 µm, 212–300 µm, 425–600 µm) for the two pressures.. The slightly elevated pressure condition coupled with the increasing spatial confinement of the plasma zone is anticipated to affect the breakdown criteria and plasma dynamics following Paschen's law [36]. Moreover, the elevated pressure condition is expected to favor the number of recombination events of methyl species (three-body reaction) (R5) relative to the number of activation events of CH_4, which should be restricted by the elevated pressure as emphasized in reaction equation (R6) where M denotes a collision partner.

$$CH_3 + H + M \rightarrow \ CH_4 + M \tag{R5}$$

$$CH_4 + e^- \rightarrow \ CH_x + (4 - x)H + e^- \tag{R6}$$

The incomplete plasma formation combined with the enhancement of recombination events of methyl species could result in a lower conversion of CH_4 for the high-pressure condition and the smallest bead sizes. This could indicate that the difference in CH_4 conversion may be associated with the higher operating pressure's ($p = 1.7$ bar) effect on the enhanced methyl recombination vs CH_4 dissociation mechanism. Lastly, it should be mentioned that the changing plasma behavior might, in principle, affect the temperature of the bulk gas in the DBD reactor and, thus, the NOCM chemistry. However, the conversion of CH_4 and the product selectivities were found to be constant and independent of the temperature in the range of 25–200 °C, as shown in Figures S14 and S15 in the SI.

The Product Distribution

Besides influencing the conversion, the product composition was also observed to change significantly with decreasing size of the glass beads. A clear increase in selectivity towards unsaturated C_2 products was observed for both pressure conditions as a function of decreasing bead size. The selectivity towards unsaturated C_2 increased substantially by ~ 25% and ~ 45% when comparing the reactor performance for the empty reactor, the packed reactor with the largest (2000–5000 μm) and smallest (150–212 μm) glass beads, for the high- and low-pressure conditions, respectively. This tendency is also suggested to be primarily a combined effect of the operating pressure and transitional plasma behavior. The dominating reaction pathways for the formation of unsaturated C_2 are proposed to be strongly dependent on the plasma behavior, as the plasma is the only activation mechanism and as the C–C coupling reactions require significant activation energy in the required initial step of H-abstraction, as seen in Table 4.

With increasing spatial confinement of the plasma zone, the small interparticle void spaces constrain the formation of a complete plasma, resulting in low-magnitude current pulses and a high degree of partial discharging. The incomplete plasma behavior is still sufficiently energetic and capable of activating CH_4 generating reactive CH_x species (R6), which can react to form stable C_2 species (R7), metastable electronically excited C_2 species, or recombine with hydrogen as the first reaction step (R5) [40, 42].

$$CH_3 + CH_3 \rightarrow C_2H_6 \tag{R7}$$

Subsequently, a second activation of stable C_2 species (ethane, ethylene, acetylene) might follow as shown previously in (R1–R4) and (R8) [40, 42].

$$C_2H_6 + e^- \rightarrow C_2H_4 + H_2 + e^- \tag{R8}$$

However, ethane has weaker C–H bonds (421 kJ/mol) in comparison to those of ethylene and acetylene (465 kJ/mol, 558 kJ/mol). Coupled with the weaker plasma for smaller beads (due to the partial discharging regime), this suggests that a higher fraction of the formed ethane, relative to the formed ethylene or acetylene, can be activated and react to form primarily unsaturated C_2 or C_3 species as previously shown in (R3) and (R4) [40, 42, 49]. However, plasma activation of ethylene or acetylene that can react with methyl and hydrogen radicals may also contribute to the formation of C_3 but these reaction pathways are anticipated to contribute less with decreasing bead size.

Table 4 Overview of the bond dissociation energies (BDE) of hydrogen for the products obtained in this study [49]

C–H BDEs	CH_3-H	CH_3CH_2–H	$H_2C=CH$–H	HC≡C–H
D°_{298}/kJ/mol	439.3	420.5	465.3	557.8

The reactions facilitating the formation of unsaturated C_2 are suggested to be marginally enhanced at the elevated pressure condition (1.7 bar), as the residence time, compared to the low-pressure condition (1.2 bar), is prolonged, increasing the probability of secondary activation events of ethane. Still, the pressure effect on the competing activation and recombination mechanisms, alongside the increasing transition towards partial discharging dynamics (exhibiting low-magnitude current pulses) observed with decreasing bead size, are suggested to be the key factor in controlling the reaction routes of NOCM. The incomplete plasma formation is expected to be insufficiently energetic to facilitate activation of the formed ethylene or acetylene, increasing the selectivity towards these compounds. As a direct result of this, the selectivity towards C_3 species decreases with decreasing bead sizes. The higher degree of partial discharging and lower current peaks, which reflect a weaker plasma, inhibit and decrease the probability of having further reactions occurring with the formed ethylene or acetylene for both pressure conditions. This effect is slightly more apparent for the elevated pressure due to the increased collision frequency, favoring recombination events of methyl, relative to the activating mechanism of methane. This lowers the concentration of methyl species available for further reactions with formed C_2 species, thus influencing the formation of C_3 species.

A simplified overview of the discussed reaction dynamics in this study and in agreement with other studies [40, 42] is provided in Fig. 12, showing the possible reaction pathways relevant for the plasma-assisted NOCM. However, substantiation by modeling would be necessary to determine and confirm the detailed reaction mechanism for the different operating conditions associated with the different glass bead systems.

Limitations of Equivalent Circuit Models

In agreement with most publications on PBR DBDs, this study confirms that partial discharging is a common phenomenon occurring in PBR DBDs, often exemplified through non-ideal almond-shaped Q–V plots, which increases the complexity of the electrical characterization of the plasma behavior [27, 38, 50–52]. The understanding and determination of reactor properties of discharge regimes rely on equivalent circuit models,

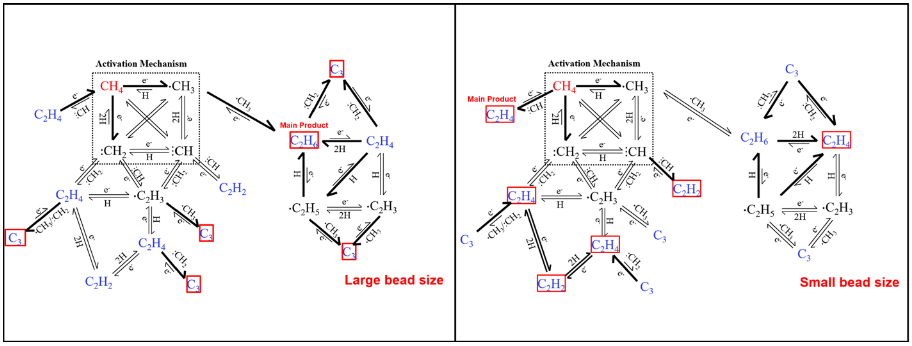

Fig. 12 A proposed simplified reaction scheme for the high-pressure condition of the possible reaction pathways for the plasma-assisted NOCM. Note that the reaction scheme only includes radical reactions. The mechanisms shown to the left and right sides show proposed reaction pathways using different bead size as indicated. The effect of the plasma dynamics and specifically degree of partial discharging on the product distribution is visualized using thick black arrows. The main products are highlight in a red box

which, as it stands, could be improved in capturing the variable breakdown voltage and varying capacitance during discharging associated with the incomplete plasma formation in PBR DBDs. Thus, the development of more extensive and accurate equivalent circuit models, accounting for the complex characteristics of the co-dependent dynamics of plasma and packing material, could provide useful information about the mechanisms of plasma formation and, thereby, the exact operating conditions of PBRs. Future circuit models should describe the intercorrelated dependency of the applied voltage, reactor porosity, and the capacitive properties of the packing material on the capacitance during discharging, to capture and quantify the non-ideality of partial discharging regimes.

In addition, there is another complexity to consider that such circuit models should be capable of describing to understand the complete mechanism. During the operation of PBR DBDs working with carbon chemistry, carbon deposition is anticipated to gradually accumulate on the surface of the packing material. This affects the electrical conductivity alongside the effect of the capacitive properties of the packing material in the plasma zone, which may influence the plasma behavior significantly. This effect is rarely addressed in the scientific literature, despite the fact that it might be highly significant for the plasma behavior and when utilizing catalytic materials that rely on surface reactions. Small amounts of carbon deposits were observed on the glass beads in this study, however, the amount or composition was not quantified or determined. Furthermore, the deposited amount of carbon was similar to oil in texture, and the deposition was so little that it did not have a measurable effect on the electrical behavior of the plasma during the experiments. As outlined, existing equivalent circuit models still face limitations in describing the complex plasma-packing material interactions. However, in the absence of the complete mathematical formalism, this study has applied the partial discharging formalism by Peeters et al. [46] coupled with the extended methodology of Butterworth et al. [36]. This combined formalism allowed for the determination of the partial discharging coefficient alpha, for the different glass bead systems, as a qualitative measure used to quantify the plasma behavior in terms of partial discharging degree. The outcomes of this study show an increase in reactor partial discharging, resulting in increasing alpha values, with increasing spatial confinement of the plasma zone for the glass beads tested under equivalent operating conditions. However, the accuracy and interpretation of the value of alpha for different packing materials is still debatable. Especially in the intermediate region ($\alpha = 0.5$), as existing literature has reported similar values of alpha for different materials despite observing, by visual inspection or analysis of voltage-current data, significant differences in the plasma behavior and dominating discharge regime [36]. This indicates that alpha can be a useful indicator in quantifying the plasma behavior, however, additional data is required to substantiate the plasma dynamics when testing and comparing the reactor performance of different packing materials. Conversely, in this study, the only packing material that was tested was glass beads for all the experiments conducted. Thus, the determined value of alpha is suggested to be a reliable parameter for the characterization of the plasma behavior and dominating discharge regime for the different glass bead systems relative to each other. In general, this approach and application of alpha is an uncommon practice in the majority of the scientific literature dealing with PBR DBDs. In this respect, it becomes rather difficult to evaluate in detail the performance of a given packing material or catalyst, as enhanced process outcomes may be either related to a significant catalytic activity of the catalyst or transitional plasma dynamics related to its physical properties or a combined effect of both [53].

Plasma Packing Interactions

The outcomes of this study illuminate the inherently complex nature of the inter-reliant dependency of the plasma and the packing material. Utilizing glass beads as the packing material, the plasma behavior and dominating discharge regime were proven strongly dependent on the applied bead size, due to the significant increase in the capacitive behavior of the plasma zone attributed to the spatial confinement. The change in plasma behavior, wherein the partial discharging degree plays an essential role due to the limited charge transfer, was proven to affect the chemistry of NOCM, raising an important question. The synergistic effects reported in the literature have previously been stated to originate from the complex interactions between the plasma and the catalyst and vice versa, however, the question is if these co-dependent effects are equally influential on the process outcomes and if they are distinguishable. In this study, the plasma dependency on the packing material was demonstrated and confirmed by the changing discharging regime, however, it should be noted that the utilized glass beads are expected to act inert on the chemistry, only affecting the plasma. On the other hand, the exact effect of the plasma exposure on catalytic materials is still debatable, especially considering the ambient operating conditions associated with NTP systems, which significantly contrast conventional thermo-catalytic approaches. Under ambient conditions, the activity of conventionally applied catalysts for methanol synthesis, ammonia synthesis, or synthesis gas production would be minimal in NTP systems, as very energy-intensive operating conditions are required [54, 55]. This tendency is also demonstrated in the academic literature, where an extensive screening of catalytic materials has been conducted for their utilization in plasma-assisted NTP systems, often showing insignificant improvements compared with pure plasma operation [10, 11, 21, 23, 24]. Under ambient conditions, the activation mechanism in NTPs relies on plasma activation. This mechanism produces a reactive mixture of short-lived species, including radicals and vibrationally excited species. The high chemical reactivity of such mixtures suggests that the chemical reactions are already occurring in the gas phase rather than on a catalytic surface. Therefore, the plasma dynamics dependency on the applied packing material, wherein the influence on the dominating discharge regime is essential, is suggested as the dictating factor controlling the chemistry utilizing ambient operating conditions. The role of the catalyst in plasma-catalytic systems still needs clarification; however, its role in working as a conventional catalyst is proposed to be of less importance, relative to its influence on the plasma and dominating discharge regime [53]. Further, its role may become increasingly important with increasing operating temperature, as such reaction conditions are more similar to those conventionally applied. In conclusion, this study recommends that emphasis should be directed towards obtaining a detailed understanding of the plasma behavior and resulting discharging mode and its dependency on the applied packing material as the resulting plasma dynamics, are suggested to be the determining factor controlling the excitation, dissociation, and ionization rates and thereby the occurring chemistry.

Conclusion

Plasma-assisted non-oxidative coupling of methane was investigated using a co-axial packed bed DBD, utilizing glass beads of five different bead size distributions (2000–5000 μm, 900–1100 μm, 425–600 μm, 212–300 μm, 150–212 μm) as the packing and compared with an empty reactor. The experiments were conducted at a constant plasma power of 30 W for two pressure conditions ($p = 1.2$ bar, $p = 1.7$ bar). The reactor performance of the empty reactor and the five tested glass bead sizes was evaluated in terms of CH_4 conversion, the product composition, and the resulting energy efficiency and explained by conducting a detailed analysis of non-ideal almond-shaped Q–V plots for electrical characterization of the resulting plasma dynamics and dominating discharge regimes.

The partial discharge coefficient (α) was determined and used as a qualitative indicator for the tested glass bead systems, to assess the extent of plasma formation and dictating discharge regime. This was further substantiated by analysis of the resulting voltage-current data. From the results of this study, it has been shown that transitional plasma dynamics, specifically the degree of partial discharging of the reactor, was found to be dependent on the spatial confinement of the plasma zone. The partial discharging degree of the reactor is shown to increase with decreasing size of the glass beads, significantly affecting the controlling reaction routes of the NOCM. As a result, the selectivity towards unsaturated C_2 species increased significantly, from 16 to 50% and 15% to 42% for the high- and low-pressure conditions, comparing the reactor performance associated with the packing of the largest (2000–5000 μm) and smallest (150–212 μm) size of the glass beads. Conversely, the increasing degree of partial discharging was found to decrease the CH_4 conversion and the energy efficiency of plasma-assisted NOCM. The CH_4 conversion decreased from 8.5% to 3.7% and 8.8% to 5.5% for the high- and low-pressure conditions. Similarly, the energy efficiencies decreased from 8.1% to 3.9% and 8.4% to 6.5% for the high- and low-pressure, exemplifying that plasma-assisted NOCM suffers from the difficult activation mechanism of CH_4. The relatively low CH_4 conversions obtained in this work are also a result of using an undiluted feed stream. In an industrial setting, an undiluted feed would allow easier downstream separation of products and unconverted CH_4. To this end, this work elucidates the importance of understanding the influence of the inherently complex nature of the co-dependent dynamics of the plasma and packing interactions, as the plasma behavior and discharging properties are proposed to control the chemistry of the NOCM under ambient reaction conditions.

Supplementary Information The online version contains supplementary material available at https://doi.org/10.1007/s11090-025-10548-1.

Acknowledgements The authors thank Danmarks Frie Forskningsfond (DFF 0217-00231B) for funding this project.v

Author Contribution T.S. Larsen wrote the main manuscript text, processed data, and prepared all figures. J.A. Andersen—review, editing, and supervision. J.M. Christensen—review, editing, and supervision. M. Østberg—review, editing, and supervision. A. Fateev—review, editing, and supervision. E. Morias—review, editing, and supervision. A. Bogaerts—review, editing, and supervision. A.D. Jensen—review, editing, and supervision. All authors reviewed the manuscript.

Funding Open access funding provided by Technical University of Denmark.

Data Availability The authors declare that the data supporting the findings of this study are available within the paper and its Supplementary Information files. Should any raw data files be needed in another format they are available from the corresponding author upon reasonable request.

Declarations

Conflict of interest The authors declare that they have no known competing financial interests or personal relationships that could have appeared to influence the work reported in this paper.

References

1. Smith O, Cattell O, Farcot E et al (2022) The effect of renewable energy incorporation on power grid stability and resilience. Sci Adv 8(9):6734
2. Van Rooij GJ, Van Den Bekerom DCM, Den Harder N et al (2015) Taming microwave plasma to beat thermodynamics in CO_2 dissociation. Faraday Discuss 183:233–248. https://doi.org/10.1039/c5fd00045a
3. Palys MJ, Daoutidis P (2022) Power-to-X: a review and perspective. Comput Chem Eng. https://doi.org/10.1016/j.compchemeng.2022.107948
4. Feijoo F, Pfeifer A, Herc L et al (2022) A long-term capacity investment and operational energy planning model with power-to-X and flexibility technologies. Renew Sustain Energy Rev. https://doi.org/10.1016/j.rser.2022.112781
5. Sun K, Ginosar DM, He T et al (2018) Progress in nonoxidative dehydroaromatization of methane in the last 6 years. Ind Eng Chem Res 57:1768–1789
6. Mcfarland E (2012) Unconventional chemistry for unconventional natural gas. Science 338:340–342. https://doi.org/10.1126/science.1226339
7. Schwach P, Pan X, Bao X (2017) Direct conversion of methane to value-added chemicals over heterogeneous catalysts: challenges and prospects. Chem Rev 117:8497–8520
8. Zhang T (2021) Recent advances in heterogeneous catalysis for the nonoxidative conversion of methane. Chem Sci 12:12529–12545
9. Górska A, Krawczyk K, Jodzis S, Schmidt-Szałowski K (2011) Non-oxidative methane coupling using $Cu/ZnO/Al_2O_3$ catalyst in DBD. Fuel 90:1946–1952. https://doi.org/10.1016/j.fuel.2010.12.023
10. Chawdhury P, Bhanudas Rawool S, Umamaheswara Rao M, Subrahmanyam C (2022) Methane decomposition by plasma-packed bed non-thermal plasma reactor. Chem Eng Sci. https://doi.org/10.1016/j.ces.2022.117779
11. Liu L, Das S, Zhang Z, Kawi S (2022) Nonoxidative coupling of methane over ceria-supported single-atom Pt catalysts in DBD plasma. ACS Appl Mater Interfaces 14:5363–5375. https://doi.org/10.1021/acsami.1c21550
12. Snoeckx R, Bogaerts A (2017) Plasma technology—a novel solution for CO_2 conversion? Chem Soc Rev 46:5805–5863. https://doi.org/10.1039/c6cs00066e
13. Whitehead JC (2019) Plasma-catalysis: is it just a question of scale? Front Chem Sci Eng 13:264–273
14. Ollegott K, Wirth P, Oberste-Beulmann C et al (2020) Fundamental properties and applications of dielectric barrier discharges in plasma-catalytic processes at atmospheric pressure. Chem Ing Tech 92:1542–1558. https://doi.org/10.1002/cite.202000075
15. Li S, Dang X, Yu X et al (2020) The application of dielectric barrier discharge non-thermal plasma in VOCs abatement: a review. Chem Eng J 388:124275
16. Ahmad F, Lovell EC, Masood H et al (2020) Low-temperature CO_2 methanation: synergistic effects in plasma-Ni hybrid catalytic system. ACS Sustain Chem Eng 8:1888–1898. https://doi.org/10.1021/acssuschemeng.9b06180
17. Zhang AJ, Zhu AM, Guo J et al (2010) Conversion of greenhouse gases into syngas via combined effects of discharge activation and catalysis. Chem Eng J 156:601–606. https://doi.org/10.1016/j.cej.2009.04.069
18. Neyts EC, Ostrikov K, Sunkara MK, Bogaerts A (2015) Plasma catalysis: synergistic effects at the nanoscale. Chem Rev 115:13408–13446. https://doi.org/10.1021/acs.chemrev.5b00362
19. Wang L, Yi Y, Wu C et al (2017) One-step reforming of CO_2 and CH_4 into high-value liquid chemicals and fuels at room temperature by plasma-driven catalysis. Angew Chem 129:13867–13871. https://doi.org/10.1002/ange.201707131
20. Zeng Y, Zhu X, Mei D et al (2015) Plasma-catalytic dry reforming of methane over γ-Al_2O_3 supported metal catalysts. Catal Today 256:80–87. https://doi.org/10.1016/j.cattod.2015.02.007

21. Andersen JA, Christensen JM, Østberg M et al (2020) Plasma-catalytic dry reforming of methane: screening of catalytic materials in a coaxial packed-bed DBD reactor. Chem Eng J. https://doi.org/10.1016/j.cej.2020.125519
22. Loenders B, Michiels R, Bogaerts A (2023) Is a catalyst always beneficial in plasma catalysis? Insights from the many physical and chemical interactions. J Energy Chem. https://doi.org/10.1016/j.jechem.2023.06.016
23. Wang A, Harrhy JH, Meng S et al (2019) Nonthermal plasma-catalytic conversion of biogas to liquid chemicals with low coke formation. Energy Convers Manag 191:93–101. https://doi.org/10.1016/j.enconman.2019.04.026
24. Sentek J, Krawczyk K, Młotek M et al (2010) Plasma-catalytic methane conversion with carbon dioxide in dielectric barrier discharges. Appl Catal B 94:19–26. https://doi.org/10.1016/j.apcatb.2009.10.016
25. Neyts EC, Bogaerts A (2014) Understanding plasma catalysis through modelling and simulation—a review. J Phys D Appl Phys. https://doi.org/10.1088/0022-3727/47/22/224010
26. Van Laer K, Bogaerts A (2017) How bead size and dielectric constant affect the plasma behaviour in a packed bed plasma reactor: a modelling study. Plasma Sources Sci Technol. https://doi.org/10.1088/1361-6595/aa7c59
27. Mei D, Zhu X, He YL et al (2015) Plasma-assisted conversion of CO_2 in a dielectric barrier discharge reactor: understanding the effect of packing materials. Plasma Sources Sci Technol. https://doi.org/10.1088/0963-0252/24/1/015011
28. Sheng Z, Kameshima S, Yao S, Nozaki T (2018) Oxidation behavior of Ni/Al_2O_3 catalyst in nonthermal plasma-enabled catalysis. J Phys D Appl Phys. https://doi.org/10.1088/1361-6463/aae17d
29. Gandhi MS, Mok YS (2015) Effect of packing materials on the decomposition of tetrafluoroethane in a packed-bed dielectric barrier discharge plasma reactor. Int J Environ Sci Technol 12:499–506. https://doi.org/10.1007/s13762-013-0415-9
30. Ray D, Subrahmanyam C (2016) CO_2 decomposition in a packed DBD plasma reactor: influence of packing materials. RSC Adv 6:39492–39499. https://doi.org/10.1039/c5ra27085e
31. Duan X, Hu Z, Li Y, Wang B (2015) Effect of dielectric packing materials on the decomposition of carbon dioxide using DBD microplasma reactor. AIChE J 61:898–903. https://doi.org/10.1002/aic.14682
32. Van Laer K, Bogaerts A (2015) Fluid modelling of a packed bed dielectric barrier discharge plasma reactor. Plasma Sources Sci Technol. https://doi.org/10.1088/0963-0252/25/1/015002
33. Van Laer K, Bogaerts A (2017) Influence of gap size and dielectric constant of the packing material on the plasma behaviour in a packed bed DBD reactor: a fluid modelling study. Plasma Process Polym 14(4–5):1600129
34. Wang W, Kim HH, Van Laer K, Bogaerts A (2018) Streamer propagation in a packed bed plasma reactor for plasma catalysis applications. Chem Eng J 334:2467–2479. https://doi.org/10.1016/j.cej.2017.11.139
35. Peeters F, Butterworth T (2019) Electrical diagnostics of dielectric barrier discharges. In: Atmospheric pressure plasma
36. Butterworth T, Allen RWK (2017) Plasma-catalyst interaction studied in a single pellet DBD reactor: dielectric constant effect on plasma dynamics. Plasma Sources Sci Technol. https://doi.org/10.1088/1361-6595/aa6c35
37. Kim J, Jeoung J, Jeon J et al (2019) Effects of dielectric particles on non-oxidative coupling of methane in a dielectric barrier discharge plasma reactor. Chem Eng J. https://doi.org/10.1016/j.cej.2018.09.057
38. Taheraslani M, Gardeniers H (2020) Coupling of CH_4 to C_2 hydrocarbons in a packed bed DBD plasma reactor: the effect of dielectric constant and porosity of the packing. Energies (Basel). https://doi.org/10.3390/en13020468
39. Taheraslani M, Gardeniers H (2020) Plasma catalytic conversion of CH_4 to alkanes, olefins and H_2 in a packed bed DBD reactor. Processes. https://doi.org/10.3390/PR8070774
40. Kechagiopoulos PN, Rogers J, Maitre PA et al (2024) Non-oxidative coupling of methane via plasma-catalysis over $M/\gamma\text{-}Al_2O_3$ catalysts (M = Ni, Fe, Rh, Pt and Pd): impact of active metal and noble gas co-feeding. Plasma Chem Plasma Process. https://doi.org/10.1007/s11090-024-10507-2
41. Andersen JA, Christensen JM, Østberg M et al (2022) Plasma-catalytic ammonia decomposition using a packed-bed dielectric barrier discharge reactor. Int J Hydrogen Energy 47:32081–32091. https://doi.org/10.1016/j.ijhydene.2022.07.102
42. De Bie C, Verheyde B, Martens T et al (2011) Fluid modeling of the conversion of methane into higher hydrocarbons in an atmospheric pressure dielectric barrier discharge. Plasma Process Polym 8:1033–1058. https://doi.org/10.1002/ppap.201100027

43. Manley TC (1943) The electric characteristics of the ozonator discharge. Trans Electrochem Soc 84(1):83
44. Ashpis DE, Laun MC, Griebeler EL (2012) Progress toward accurate measurements of power consumptions of DBD plasma actuators. In: 50th AIAA aerospace sciences meeting including the new horizons forum and aerospace exposition
45. Umamaheswara Rao M, Bhargavi KVSS, Chawdhury P et al (2023) Non-thermal plasma assisted CO_2 conversion to CO: influence of non-catalytic glass packing materials. Chem Eng Sci. https://doi.org/10.1016/j.ces.2022.118376
46. Peeters FJJ, Van De Sanden MCM (2015) The influence of partial surface discharging on the electrical characterization of DBDs. Plasma Sources Sci Technol. https://doi.org/10.1088/0963-0252/24/1/015016
47. Butterworth T, Elder R, Allen R (2016) Effects of particle size on CO_2 reduction and discharge characteristics in a packed bed plasma reactor. Chem Eng J 293:55–67. https://doi.org/10.1016/j.cej.2016.02.047
48. Valdivia-Barrientos R, Pacheco-Sotelo J, Pacheco-Pacheco M et al (2006) Analysis and electrical modelling of a cylindrical DBD configuration at different operating frequencies. In: Plasma sources science and technology, pp 237–245
49. Lide DR (2005) Handbook of chemistry and physics, 86th edn. CRC Press, Boca Raton
50. Dou B, Bin F, Wang C et al (2013) Discharge characteristics and abatement of volatile organic compounds using plasma reactor packed with ceramic Raschig rings. J Electrostat 71:939–944. https://doi.org/10.1016/j.elstat.2013.08.003
51. Tu X, Gallon HJ, Twigg MV et al (2011) Dry reforming of methane over a Ni/Al_2O_3 catalyst in a coaxial dielectric barrier discharge reactor. J Phys D Appl Phys. https://doi.org/10.1088/0022-3727/44/27/274007
52. Gómez-Ramírez A, Montoro-Damas AM, Cotrino J et al (2017) About the enhancement of chemical yield during the atmospheric plasma synthesis of ammonia in a ferroelectric packed bed reactor. Plasma Process Polym. https://doi.org/10.1002/ppap.201600081
53. Ndayirinde C, Gorbanev Y, Ciocarlan RG et al (2023) Plasma-catalytic ammonia synthesis: packed catalysts act as plasma modifiers. Catal Today. https://doi.org/10.1016/j.cattod.2023.114156
54. Sehested J (2019) Industrial and scientific directions of methanol catalyst development. J Catal 371:368–375
55. Kandemir T, Schuster ME, Senyshyn A et al (2013) The Haber–Bosch process revisited: on the real structure and stability of “ammonia iron” under working conditions. Angew Chem Int Edn 52:12723–12726. https://doi.org/10.1002/anie.201305812

Plasma-assisted non-oxidative coupling of methane: Effects of bead size distribution and operating pressure in a co-axial DBD supporting information

T. S. Larsen [1], J. A. Andersen[1], J. M. Christensen [1], A. Fateev [1], M. Østberg [2], E. Morais [3], A. Bogaerts [3], A. D. Jensen [1,*]
[1] Department of Chemical and Biochemical Engineering, Technical University of Denmark, Kgs. Lyngby, Denmark
[2] Topsoe A/S, Denmark, Kgs. Lyngby, Denmark
[3] PLASMANT, Department of Chemistry, University of Antwerp, Wilrijk, Belgium
* Corresponding author: Aj@kt.dtu.dk (A.D. Jensen)

S1. Experimental section: A detailed methodology description

1.1 Conversion and selectivity

The methane flow rate (Nml/min) into the reactor was measured before every experiment using a bubble flow meter. Further, the inlet concentration of methane was determined on the GC by sampling at least 3 times before the start of every experiment. The total flow out of the reactor was calculated by adding a small flow of nitrogen (8 ml/min) between the reactor outlet and the inlet to the GC as an internal standard. From the nitrogen flow and corresponding calibration curve, the total flow out of the reactor was calculated based on the concentration of nitrogen measured on the GC. The molar flow rates of the different species were determined on the basis of the internal standard of the nitrogen flow. This allowed the calculation of the conversion of CH_4 and carbon selectivity of the different species according to Equations (S.1) and (S.2), i.e., the equations as shown in the main text.

$$X_{CH_4}(\%)=\frac{F_{in,CH_4}-F_{out,CH_4}}{F_{in,CH_4}}\cdot 100\% \tag{S.1}$$

$$S_{C_xH_y}(\%)=\frac{x\cdot F_{C_xH_y}}{F_{in,CH_4}-F_{out,CH_4}}\cdot 100\% \tag{S.2}$$

The GC was calibrated with a calibration gas containing C_2H_6, C_2H_4, C_2H_2, C_3H_8, C_3H_6, and C_4H_{10}. In the chromatographic analysis of the product stream from the reactor, the initial temperature of the oven in the GC was 35 °C, where the sample was held for 1 minute. Afterward, the oven temperature was increased at a rate of 10 °C/min for 15.5 minutes giving a final temperature of 180 °C.

1.2 Packing materials and packing of reactor

The reactor was always packed with a fresh packing of glass beads before every experiment except in the case of the empty reactor experiments. As shown in Figure 1 in the main text, the glass beads were held in place by glass wool. Initially, when the reactor had to be packed, the inner stainless steel electrode was centered in the reactor by glass wool, then the reactor was held in a vertical position to fill in the glass beads, and finally, glass wool was placed to end the plasma zone and fixate the glass beads. During the filling of the beads, a ruler was used to measure the zone to be 5 cm long. A subsequent compression of the packing was handled using a thin metal rod that could fit in the discharge gap. A photo of the packed reactor before and after the plasma experiments is shown in Figure S1.

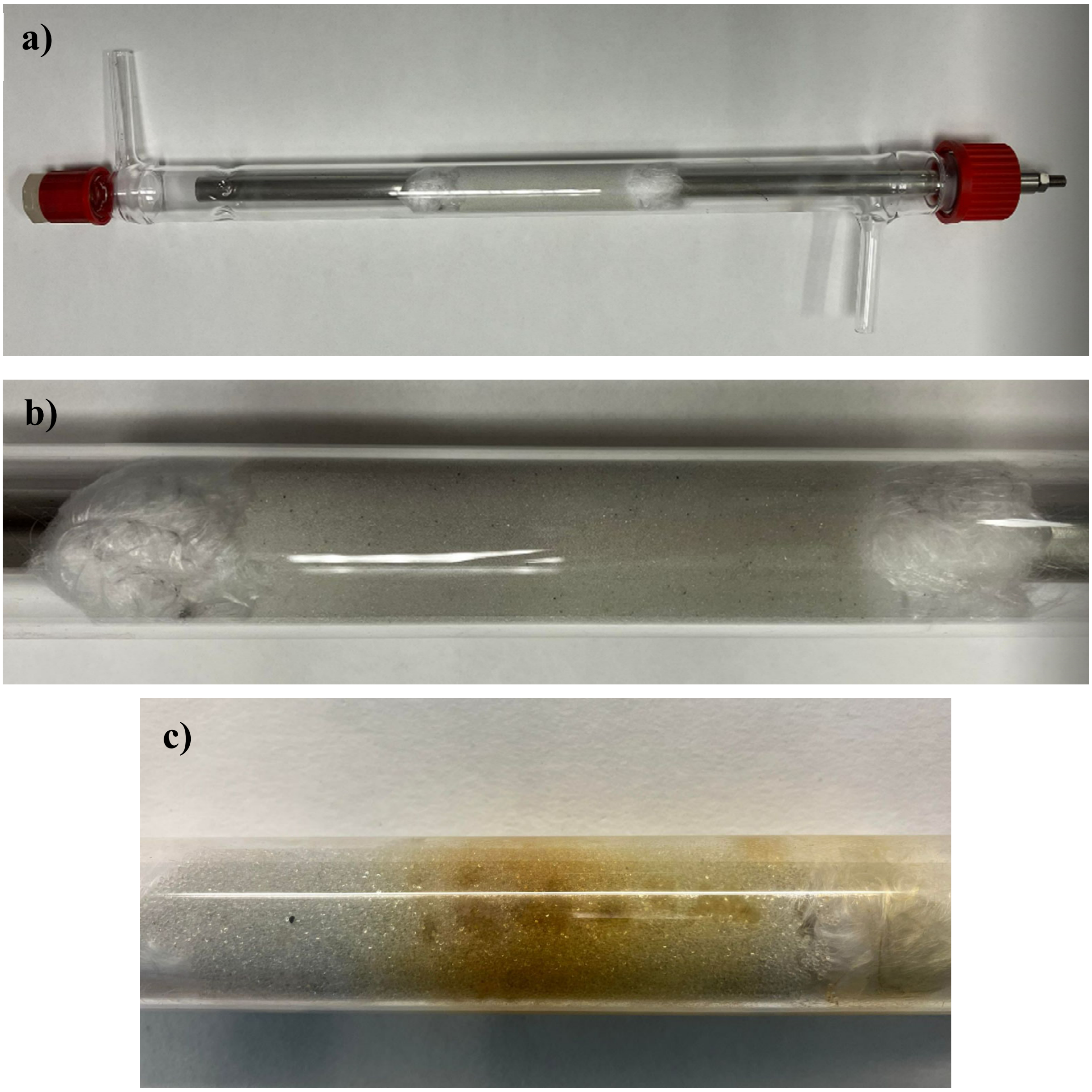

Figure S1 – a) Photographic documentation showing a) the packed DBD reactor before the plasma-assisted NOCM experiment, b) a magnification of the fresh glass beads, c) a magnification of the spent glass beads showing carbon deposition on the beads.

The packing porosity for the different bead sizes was estimated by calculating the volume of the void in the reactor for the different bead sizes and taking that void volume relative to the volume of the empty plasma zone (V_{void}/V_{total}). This was done according to the following procedure. Firstly, the beads were weighed (m_{bead}) and subsequently filled in the reactor. Secondly, it was measured how long a distance (L_{zone}) the weighed amount of beads was occupying in the annulus. Thirdly, the volume occupied by beads in the reactor was estimated using the density of SiO_2 (ρ_{SiO2}=2634 kg/m^3) as shown in Equation (S.3).

$$V_{bead}=\frac{m_{bead}}{\rho_{SiO_2}} \tag{S.3}$$

The volume of the empty annulus is expressed according to Equation (S.4)

$$V_{total}=\pi\cdot\left(r_{i.d}^{2}-r_{electrode}^{2}\right)\cdot L_{zone} \tag{S.4}$$

where $r_{i.d}$ is the inner diameter of the quartz glass reactor (19 mm), $r_{electrode}$ is the diameter of the inner stainless steel electrode (10 mm), and L_{zone} is the length of the cylinder occupied by the beads. The volume of the void (V_{void}) in the reactor was then estimated as the difference between V_{total} and V_{bead} as shown in Equation (S.5).

$$V_{void}=V_{total}-V_{bead} \tag{S.5}$$

Thus, the packing porosity was estimated according to Equation (S.6).

$$\varepsilon_{packing}=\frac{V_{void}}{V_{total}} \tag{S.6}$$

The results for the different packing porosities are presented in Table 2 in the main text.

1.3 Residence time

The residence time for the empty reactor is calculated according to Equation (S.7)

$$\tau=\frac{V_{plasma\ zone}}{v_0} \tag{S.7}$$

where $V_{plasma\ zone}$ is the volume of the annulus for the 5 cm long plasma zone, and v_0 is the volumetric flow rate of CH_4 of 50 Nml/min. For the packed reactor, τ was corrected with packing porosity, as seen in Equation (S.8).

$$\tau=\frac{V_{plasma\ zone}}{v_0}\cdot\varepsilon_{packing} \tag{S.8}$$

For the slightly elevated pressure condition, τ was corrected with the increase in pressure from the ideal gas law as justified in Equation (S.9).

$$\tau=\frac{V_{plasma\ zone}}{\frac{P_0}{P}\cdot v_0}\cdot\varepsilon_{packing} \tag{S.9}$$

where P_0 is the ambient pressure of 1.2 bar, and P is the elevated pressure of 1.7 bar.

1.4 Estimation of hydrogen

The molar flow of hydrogen (F_{H2}) in Equation (4) in the main text was estimated based on the stoichiometry of the following reactions (S.R1-S.R3) since the molar flows of the products were determined.

$$2\ CH_4 \rightarrow C_2H_4 + 2\ H_2 \tag{S.R1}$$

$$2\ CH_4 \rightarrow C_2H_6 + H_2 \tag{S.R2}$$

$$3\ CH_4 \rightarrow C_3H_8 + 2\ H_2 \tag{S.R3}$$

The estimated molar flow of hydrogen corresponds to the worst-case scenario, considering that unsaturated C_2 was assumed to only consist of C_2H_4 and C_3 only to comprise C_3H_8 yielding the lowest molar flow of hydrogen. This was done to prevent an overestimation of the energy efficiency factor.

1.5 Plasma power measurements

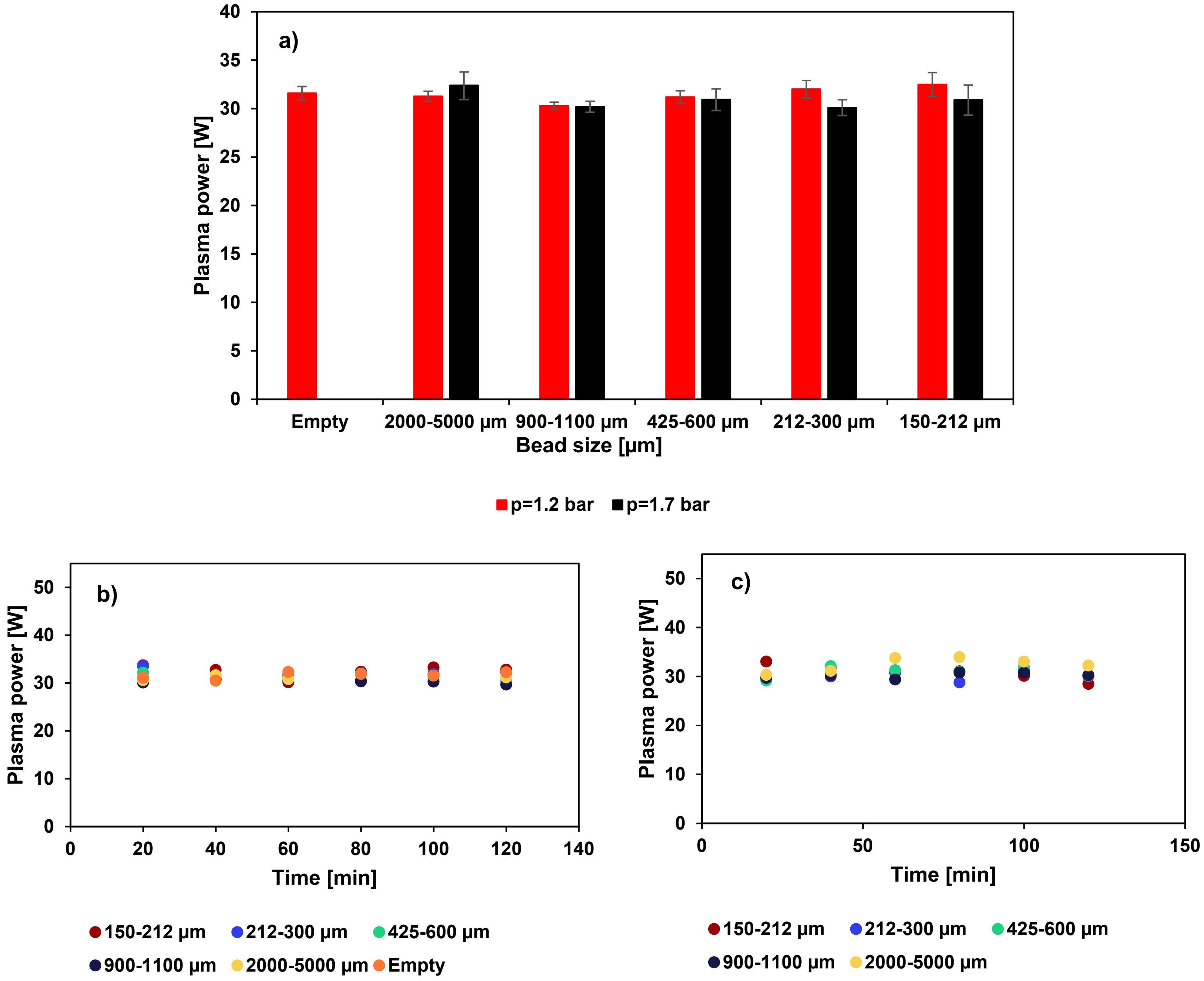

Figure S2 – a) Average plasma power for the different bead sizes and empty reactor for the two pressure conditions. Plasma power as a function of time on stream for a) the low-pressure conditions and b) the high-pressure condition for the different bead sizes and the empty reactor.

S2. Conversion of CH_4 and selectivities for the high-pressure condition p=1.7 bar

The Figures (S3-S6) shown in this section, the time t=0 min on the x-axis corresponds to the start of the experiment after the 30 min of plasma stabilization.

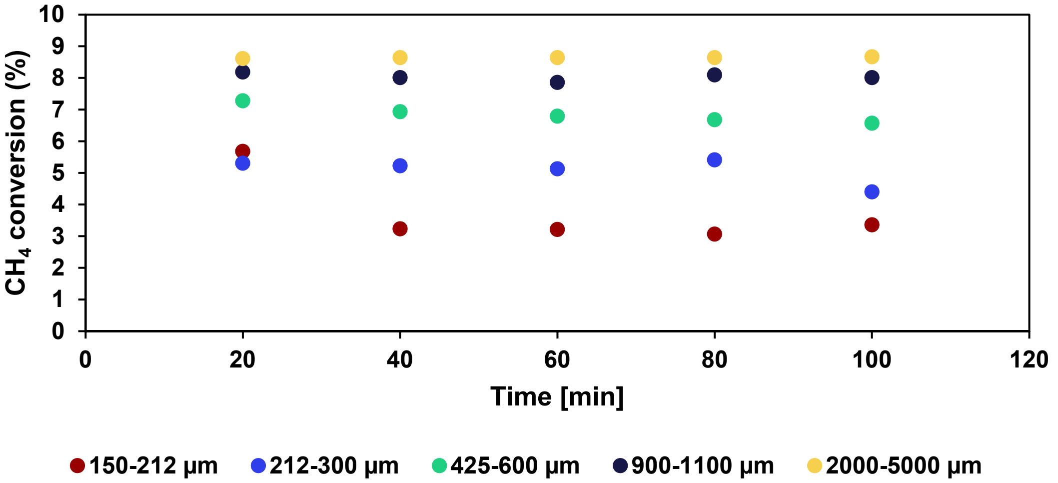

Figure S3 - CH_4 conversion as a function of time on stream. P=30 W, operating pressure=1.7 bar, flow=50 Nml/min, f= 3 kHz, outer electrode length=5 cm, inner electrode diameter=10 mm, reactor inner diameter=19 mm.

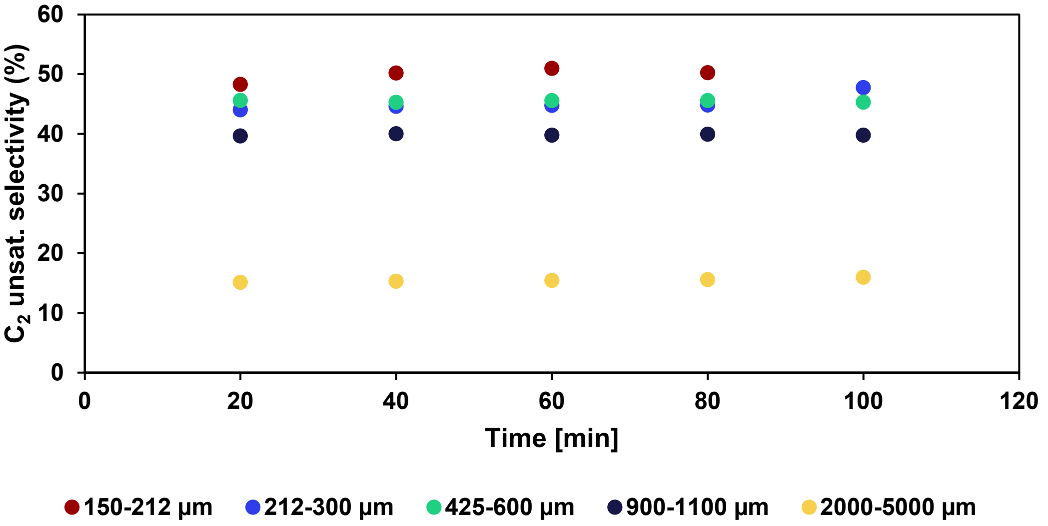

Figure S4 - C_2 unsat. selectivity as a function of time on stream. P= 30 W, operating pressure=1.7 bar, flow=50 Nml/min, f=3 kHz, outer electrode length=5 cm, inner electrode diameter=10 mm, reactor inner diameter=19 mm.

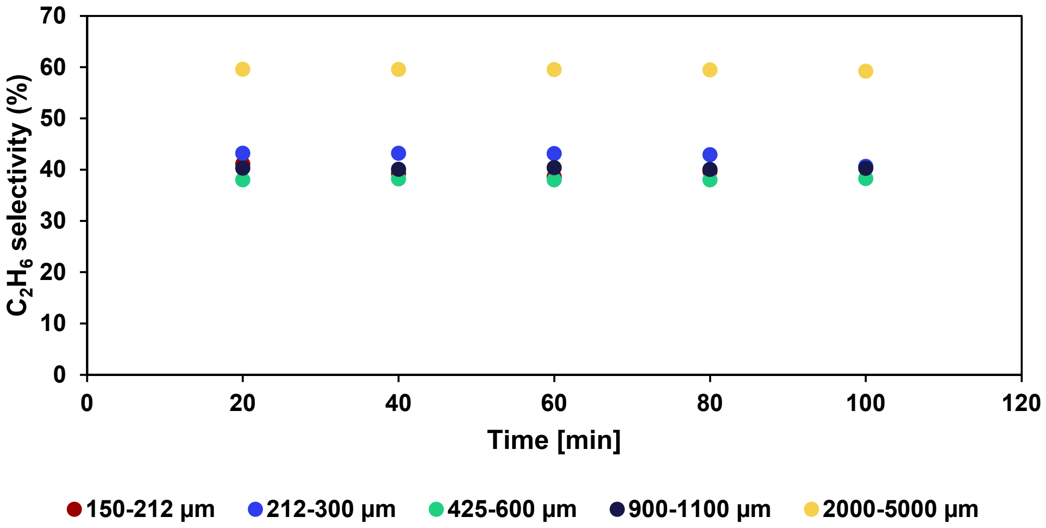

Figure S5 - C_2H_6 selectivity as a function of time on stream. P=30 W, operating pressure=1.7 bar, flow=50 Nml/min, f=3 kHz, outer electrode length=5 cm, inner electrode diameter=10 mm, reactor inner diameter=19 mm.

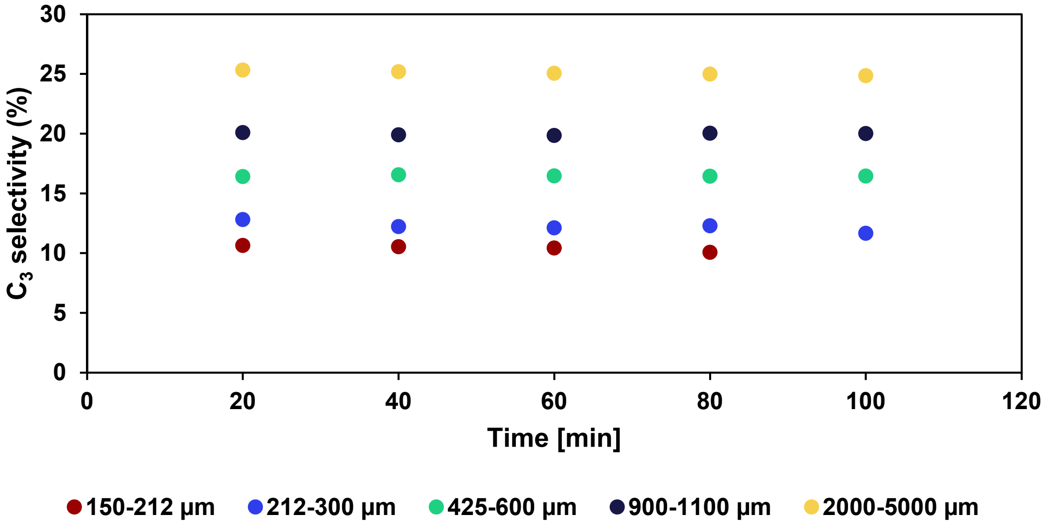

Figure S6 - C_3 selectivity as a function of TOS. P=30 W, operating pressure=1.7 bar, flow=50 Nml/min, f=3 kHz, outer electrode length=5 cm, inner electrode diameter=10 mm, reactor inner diameter=19 mm.

S3. Conversion of CH_4 and selectivities for the low-pressure condition p=1.2 bar

In Figures (S7-S10) shown in this section, the time t=0 min on the x-axis corresponds to the start of the experiment after the 30 min of plasma stabilization.

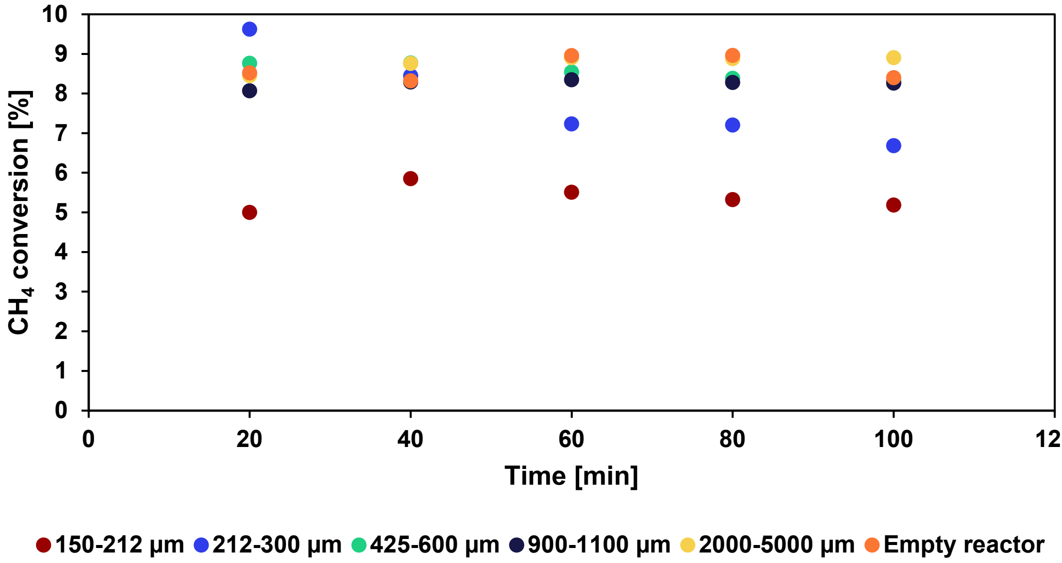

Figure S7 - CH_4 conversion as a function of time on stream. P=30 W, operating pressure=1.2 bar, flow=50 Nml/min, f=3 kHz, outer electrode length=5 cm, inner electrode diameter=10 mm, reactor inner diameter=19 mm.

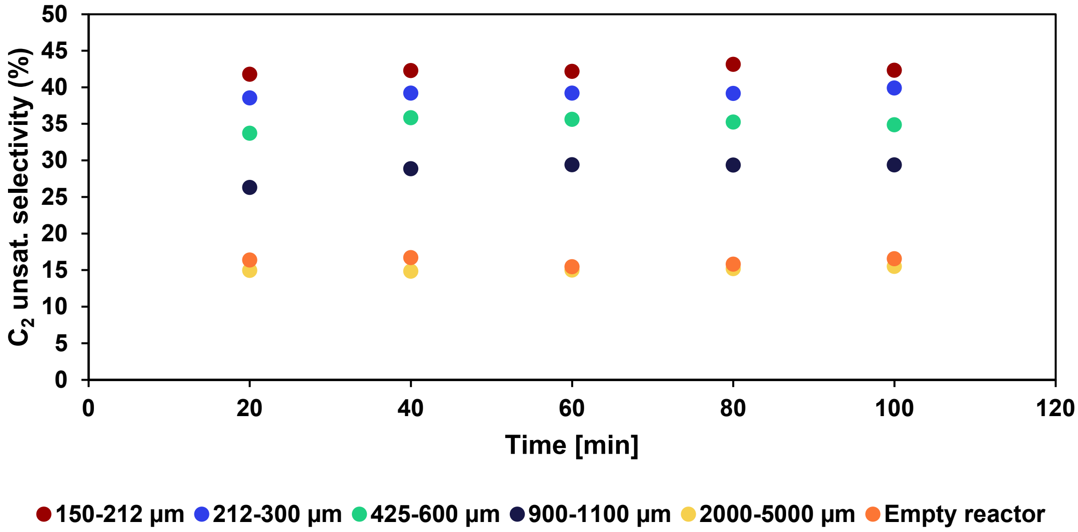

Figure S8 - C_2 unsat. selectivity as a function of time on stream. P=30 W, operating pressure=1.2 bar, flow=50 Nml/min, f=3 kHz, outer electrode length=5 cm, inner electrode diameter=10 mm, reactor inner diameter=19 mm.

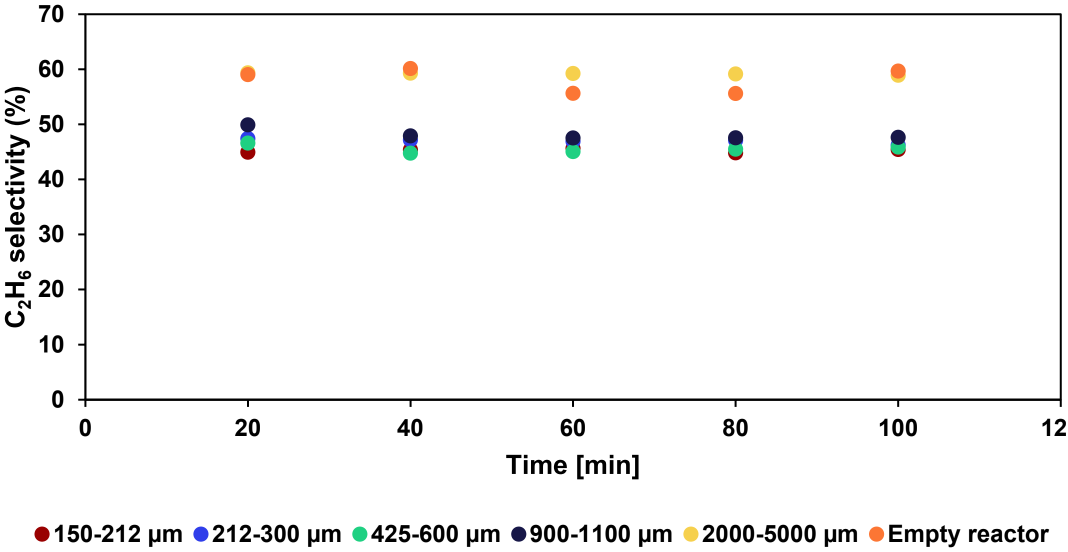

Figure S9 - C_2H_6 selectivity as a function of time on stream. P=30 W, operating pressure=1.2 bar, flow=50 Nml/min, f=3 kHz, outer electrode diameter=5 cm, inner electrode diameter=10 mm, reactor inner diameter=19 mm.

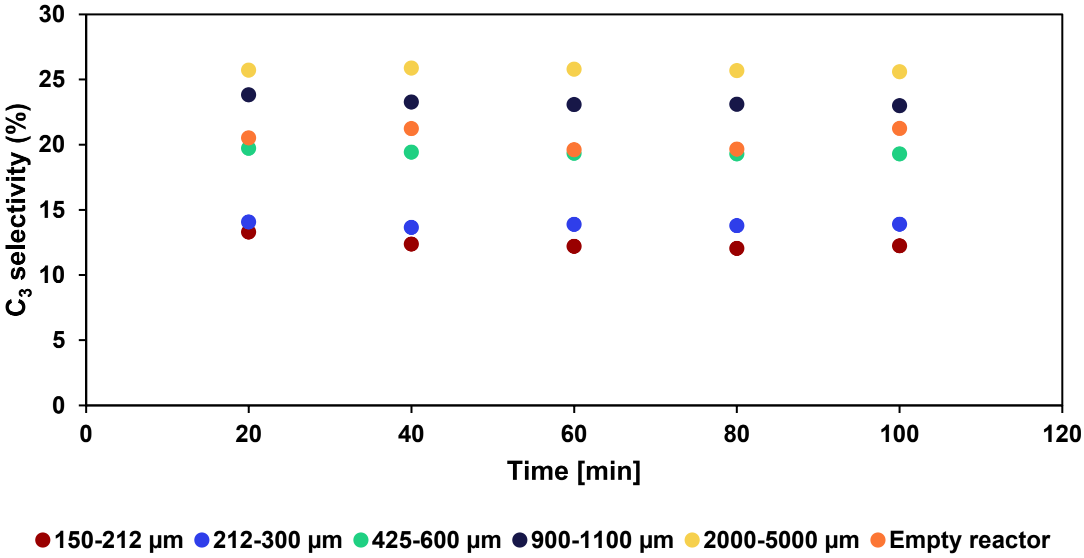

Figure S10 - C_3 selectivity as a function of time on stream. P=30 W, operating pressure=1.2 bar, flow=50 Nml/min, f=3 kHz, outer electrode length=5 cm, inner electrode diameter=10 mm, reactor inner diameter=19 mm.

Table S1 – Overview of the selectivities of the saturated and unsaturated C_2 species obtained for the two pressure conditions for the different glass bead sizes and the empty reactor.

Glass Bead Distribution, [µm]	**S(unsat. C_2), [%]**		**S(sat. C_2), [%]**	
	p=1.7 bar	**p=1.2 bar**	**p=1.7 bar**	**p=1.2 bar**
150-212	**50**	**42**	**40**	**45**
212-300	**45**	**39**	**42**	**47**
425-600	**45**	**35**	**38**	**46**
900-1100	**40**	**29**	**40**	**48**
2000-5000	**16**	**15**	**59**	**59**
Empty	**--**	**16**	**--**	**59**

S4. Electrical characterization for the low-pressure condition p=1.2 bar

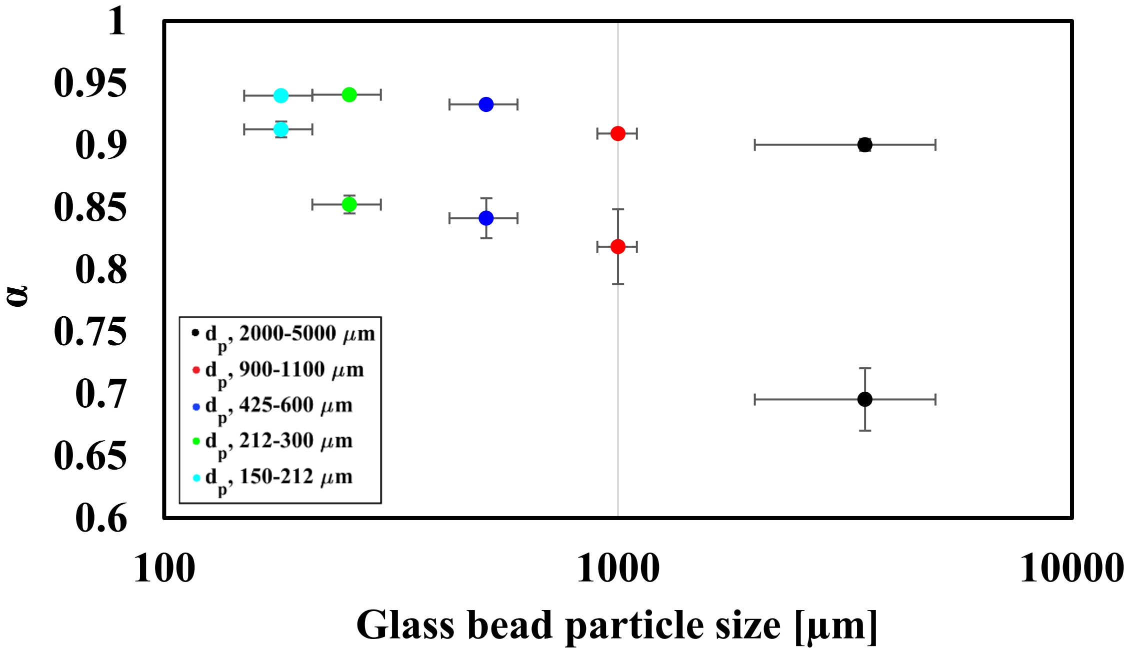

Figure S11 - Estimated interval ranges for resulting α value for the low-pressure condition. P=30 W, operating pressure=1.2 bar, flow=50 Nml/min, f=3 kHz, outer electrode length=5 cm, inner electrode diameter=10 mm, reactor inner diameter=19 mm.

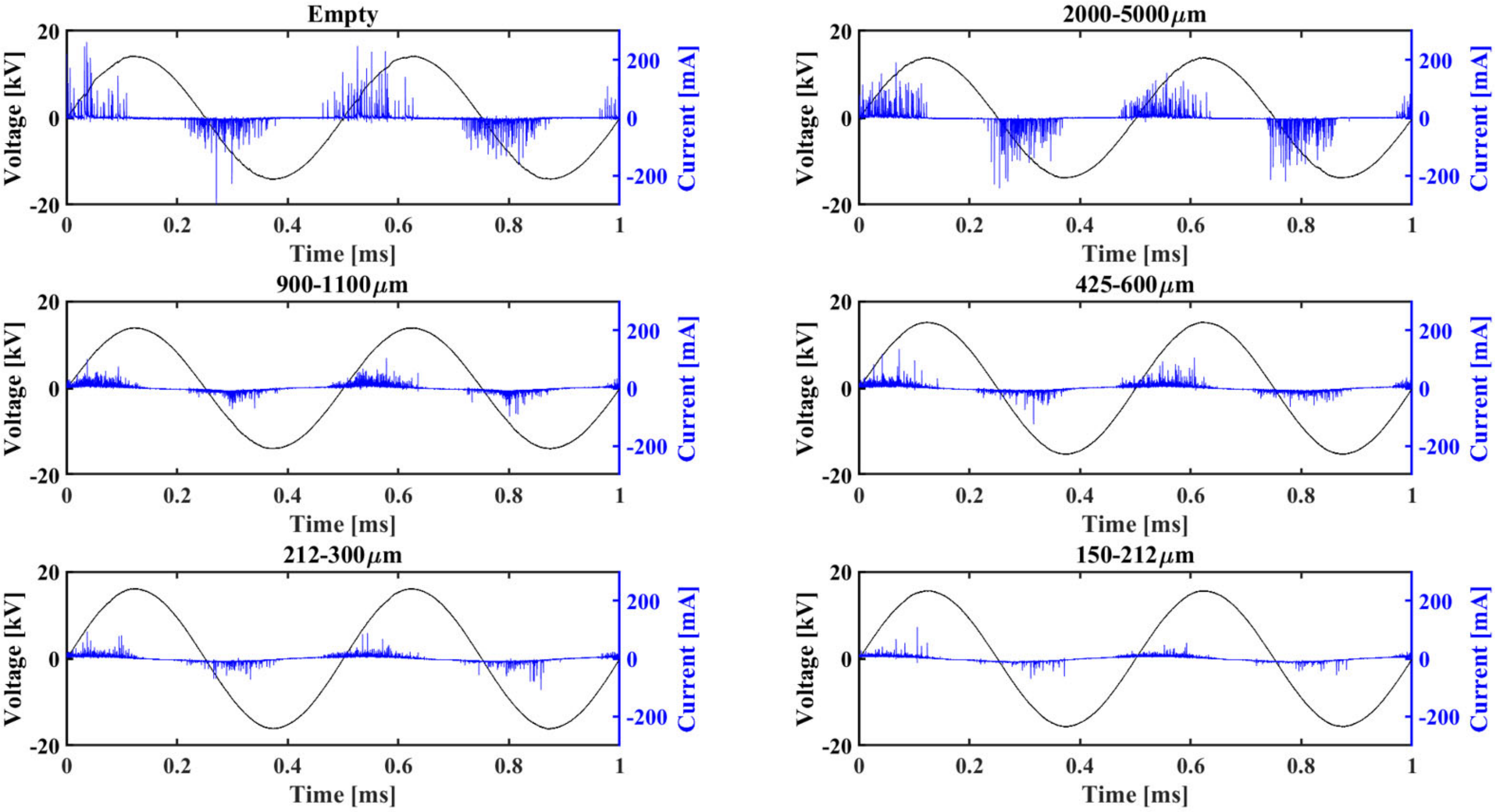

Figure S12 - Voltage-current characteristics for the tested glass beads systems measured after 40 min run time for the low-pressure condition (1.2 bar). The presented discharge characteristics have been filtered with a 20-point Savitzky-Golay filter to remove any unnecessary noise. P=30 W, operating pressure=1.2 bar, flow=50 Nml/min, f=3 kHz, outer electrode length=5 cm, inner electrode diameter=10 mm, reactor inner diameter=19 mm.

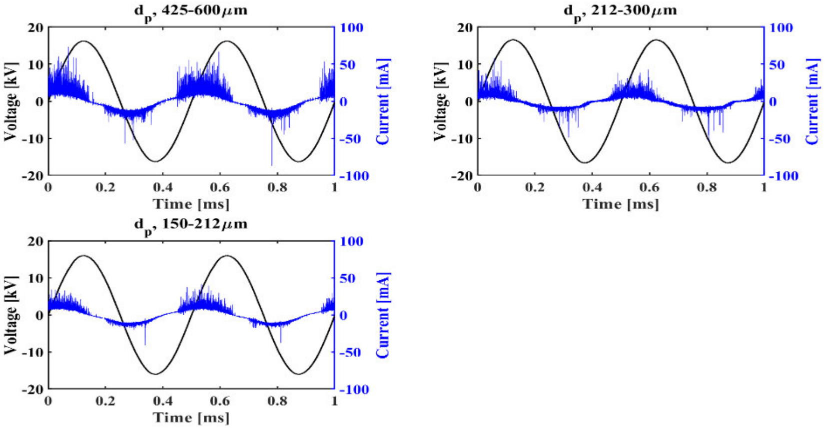

Figure S13 - Magnification of the three smallest bead size distributions (150-212 µm, 212-300 µm, and 425-600 µm) for the high-pressure condition. The presented discharge characteristics have been filtered with a 20-point Savitzky-Golay filter to remove any unnecessary noise.

The calculation of the dielectric capacitance is shown in Equation (S.10).

$$C_{\mathrm{diel}}=\frac{2\pi\cdot 8.854\times 10^{-12}\,\frac{\mathrm{F}}{\mathrm{m}}\cdot 3.76\cdot 5\times 10^{-2}\,\mathrm{m}}{\ln\left(\frac{9.5\times 10^{-3}\,\mathrm{m}+1.5\times 10^{-3}\,\mathrm{m}}{9.5\times 10^{-3}\,\mathrm{m}}\right)}=7.134\times 10^{-11}\ \mathrm{F} \qquad \text{(S.10)}$$

Table S2 – Extracted capacitances from the Lissajous figures for the different bead sizes and the empty reactor.

	2000-5000 μm		900-1100 μm		425-600 μm		212-300 μm		150-212 μm		Empty
Capacitance	p=1.2 bar	p=1.7 bar	p=1-2 bar	p=1.7 bar	p=1-2 bar	p=1.7 bar	p=1-2 bar	p=1.7 bar	p=1-2 bar	p=1.7 bar	p=1-2 bar
C_{Cell} [F]	9.73×10^{-12}	8.22×10^{-12}	1.93×10^{-11}	1.81×10^{-11}	1.64×10^{-11}	1.79×10^{-11}	1.95×10^{-11}	1.71×10^{-11}	2.14×10^{-11}	2.09×10^{-11}	7.69×10^{-12}
ζ_{diel}[F]	2.26×10^{-11}	2.20×10^{-11}	2.71×10^{-11}	2.44×10^{-11}	2.24×10^{-11}	2.37×10^{-11}	2.52×10^{-11}	2.14×10^{-11}	2.54×10^{-11}	2.39×10^{-11}	2.38×10^{-11}
C_{gap} [F]	1.13×10^{-11}	9.30×10^{-12}	2.65×10^{-11}	2.42×10^{-11}	2.13×10^{-11}	2.40×10^{-11}	2.69×10^{-11}	2.25×10^{-11}	3.06×10^{-11}	2.96×10^{-11}	8.62×10^{-12}

S5. Temperature effects

As depicted in Figure S14, a few plasma-assisted NOCM experiments were conducted using external heating around the DBD reactor. These experiments were conducted using the exact same plasma setup, DBD reactor, and operating conditions (Table 1 in the main text), similar to all the other conducted plasma-assisted NOCM experiments. These experiments were conducted to elucidate whether the decreasing CH_4 conversion for decreasing bead size could be convoluted to temperature differences associated with the changing plasma behavior. The plasma zone was placed inside a heating jacket that is 17 cm long and has a diameter of 10 cm. To ensure agreement between the reactor temperature and the chosen set point of the heating jacket, a thermocouple was placed in the center of the reactor. The temperature was measured in the reactor in the plasma zone without packing using a small flow of nitrogen (25 Nml/min) with the plasma turned off. These temperature measurements are shown in Figure S15.

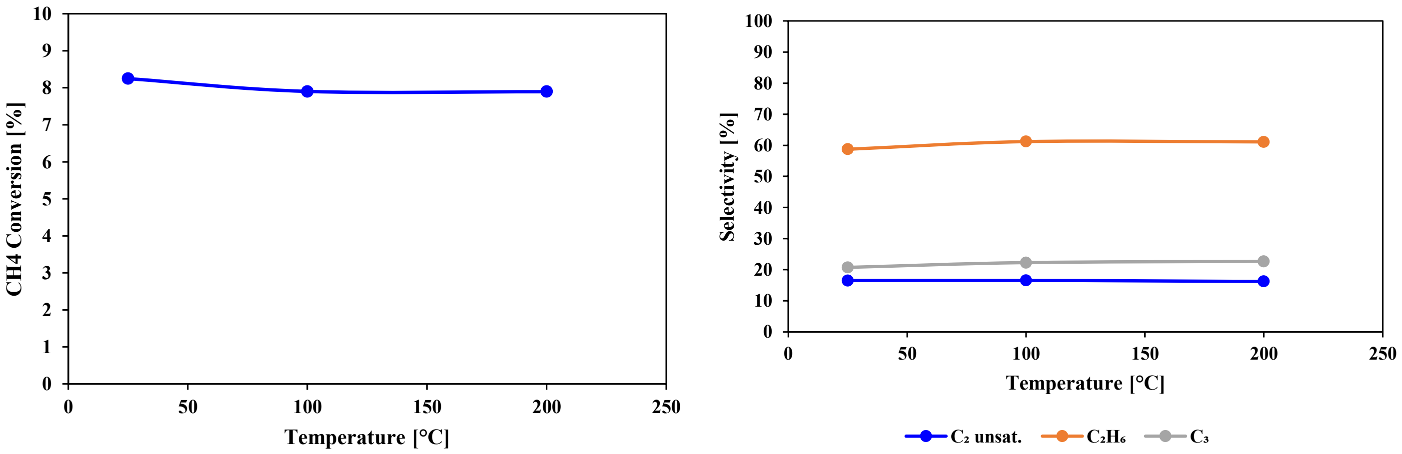

Figure S14 – a) CH_4 conversion as a function of the reactor temperature utilizing a heating jacket around the plasma zone. b) Product selectivity as a function of the reactor temperature. The data shown in this figure is for an empty reactor.

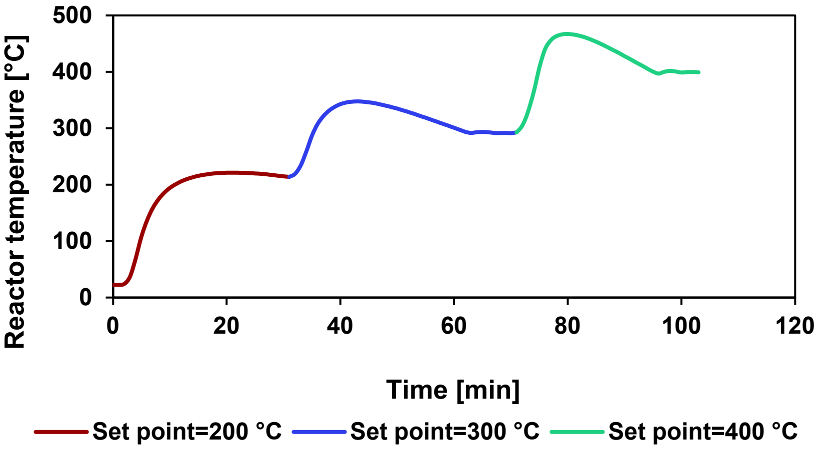

Figure 15 – Measured reactor temperature as a function of time. The thermocouple was placed inside the reactor in the plasma zone for an empty reactor with the plasma turned off to measure the temperature using a small nitrogen flow of 25 Nml/min.